Applied Surface Science 341 (2015) 149–156

Contents lists available at ScienceDirect

Applied Surface Science

journal homepage: www.elsevier.com/locate/apsusc

Amorphous nickel/cobalt tungsten sulfide electrocatalysts for high-efficiency hydrogen evolution reaction

Lun Yang[a], Xinglong Wu[a,b,*], Xiaoshu Zhu[c], Chengyu He[a], Ming Meng[a], Zhixing Gan[a], Paul K. Chu[d]

[a] Key Laboratory of Modern Acoustics, MOE, Institute of Acoustics and Collaborative Innovation Center of Advanced Microstructures, National Laboratory of Solid State Microstructures, Nanjing University, Nanjing 210093, PR China
[b] Department of Physics, NingBo University, NingBo 315001, PR China
[c] Center for Analysis and Testing, Nanjing Normal University, Nanjing 210093, PR China
[d] Department of Physics and Materials Science, City University of Hong Kong, Tat Chee Avenue, Kowloon, Hong Kong, PR China

ARTICLE INFO

Article history:
Received 24 January 2015
Received in revised form 2 March 2015
Accepted 4 March 2015
Available online 13 March 2015

Keywords:
Nickel
Cobalt
Amorphous tungsten sulfide
Hydrogen evolution

ABSTRACT

The hydrogen evolution reaction (HER), an appealing solution for future energy supply, requires efficient and inexpensive electrocatalysts with abundant active surface sites. Although crystalline MoS_2 and WS_2 are promising candidates, their activity is dominated by edge sites. Amorphous tungsten sulfide prepared so far lacks the required active sites and its application has thus been hampered. In this work, nickel and cobalt incorporated amorphous tungsten sulfide synthesized by a thermolytic process is demonstrated to enhance the HER efficiency dramatically. The amorphous nickel tungsten sulfide (amorphous NiWS) annealed at 210 °C delivers the best HER performance in this system boasting a Tafel slope of 55 mV per decade and current density of 8.6 mA cm^{-2} at 250 mV overpotential in a sustained test for 24 h. The introduction of Ni or Co into the catalyst and subsequent thermal treatment alters the porous structure and chemical bonding states thereby increasing the density of active sites on the surface.

1. Introduction

Hydrogen produced by electrolysis or solar-driven water splitting offers an environmentally acceptable and technologically promising approach to fulfill future energy demand [1–3]. Platinum group metals are the most electroactive catalysts but their rareness limits the applicability. Recently, transition-metal dichalcogenides MX_2 (M = Mo, W; X = S, Se) have drawn much attention as efficient and low-cost catalysts [4–8]. MX_2 is a bio-inspired catalyst [9] and has been used in the hydrotreating (HDT) process [10]. Containing Fe, Ni, Mo, S in the active sites, hydrogenases and nitrogenases exhibit excellent HER activity [11]. Many HDT catalysts such as molybdenum carbide [12,13], molybdenum nitride [13], tungsten carbide [14], tungsten carbonitride [15], and nickel phosphide [16] are good HER candidates [10]. These electrocatalysts also have potentials as photocatalysis and photoelectrocatalysis [17–21]. 2H-MX_2 is a general phase and the edge sites in lieu of the inert (0 0 0 1) basal planes have been identified experimentally and theoretically to be catalytically active. This indicates the importance of uncoordinated centers [9,22].

In order to achieve better performance, much effort has recently been made to produce various MX_2-based catalysts by taking advantage of the edge sites on nanosheets [23,24], double-gyroid networks [25], and molecular mimicking systems [26]. Particularly, crystalline WS_2 nanoribbons [27], WS_2 nanosheets produced by ball-milling method [28], and WS_2 nanoflakes prepared by sonochemistry [29] or solution-phase method [30] expose dense edge sites. It has been shown that the WS_2/Au hybrid [31] and WS_2/graphene hybrid produced by hydrothermal reaction [32] or electrodeposition [33] can facilitate charge transport. WS_2 nanosheets prepared by lithium intercalation [34] or microwave-assisted reaction [35] display impressing HER efficiency due to the existence of strained metallic 1T-WS_2. Crystalline catalyst is usually more stable and it is relatively easy to elucidate the catalytic mechanism compared to that of amorphous materials [8,22]. However, amorphous materials have a high concentration of unsaturated sites and can yield high activity with the proper structure [36,37]. Recently, amorphous molybdenum sulfide (MoS_x) has been shown to be an effective HER catalyst by electro-deposition [38],

* Corresponding author at: Key Laboratory of Modern Acoustics, MOE, Institute of Acoustics and Collaborative Innovation Center of Advanced Microstructures, National Laboratory of Solid State Microstructures, Nanjing University, Nanjing 210093, PR China. Tel.: +86 025 83686303; fax: +86 025 83595535.
E-mail address: hkxlwu@nju.edu.cn (X. Wu).

http://dx.doi.org/10.1016/j.apsusc.2015.03.018
0169-4332/

wet chemistry [39], heat treatment [40], and other techniques [41,42]. Similar fabrication procedures have been employed to produce crystalline [33,43] or amorphous tungsten sulfide (WS_x) [44], but the amorphous products show poor HER performance [44,45].

Considering the nickel center in hydrogenase [11] and extensive use of Ni and Co as promotional elements for 2H-MS_2 (M = Mo, W) in hydrodesulfurization (HDS) [5,10,46,47], we fabricate amorphous nickel and cobalt tungsten sulfides by a simple thermolysis process at low temperature in this work and the amorphous structure is demonstrated to be highly active for HER. The Ni^{2+} or Co^{2+} cations can interact with tetrathiomolybdate or tetrathiotungstate anions (MS_4^{2-}) to form complexes like $[M'(MS_4)_2]^{n-}$ or $M'MS_4$ (M′ = Ni, Co; M = Mo, W; n = 2, 3) which exhibit strong $M' \rightarrow MS_4$ electron delocalization [48–52]. Hence, Ni/Co incorporation and thermal treatment can be implemented together to optimize the amorphous structure. Our results reveal that although the undoped catalyst shows slow HER kinetics, the modified catalyst film with a porous morphology and larger density of active surface sites exhibits enhanced catalytic activity. By adopting the optimal synthesis conditions, the HER performance is comparable to that of crystalline WS_2 and metal pyrite families [53].

2. Experimental

2.1. Materials

Unless otherwise stated, the reagents were purchased from Sinopharm Chemical Reagent Co., Ltd. and used without further purification.

2.2. Electrode pretreatment

The fluorine-doped tin oxide electrode (FTO-coated glass, Nippon Sheet Glass, 14 Ω/sq) was cleaned in a bath containing isopropanol and then thoroughly rinsed with acetone, deionized water, and ethanol prior to use. The glassy carbon (GC, Tianjin Aidahengsheng Technology Co., 2 cm × 1 cm) substrate was polished with 1.0 μm alpha alumina and 0.05 μm gamma alumina powders (CH Instrument) suspended in de-ionized water on a Microcloth polishing pad (CH Instruments). The GC electrode was treated in an ultrasonic bath of deionized water and ethanol for 15 min.

2.3. Sample preparation

The catalyst films were synthesized by thermolysis in a CVD furnace under nitrogen atmosphere at different temperatures. In a typical procedure to prepare the amorphous nickel tungsten sulfide, 0.345 mmol (120.0 mg) of ammonium tetrathiotungstate [$(NH_4)_2WS_4$, Alfa Aesar] and 0.115 mmol (27.3 mg) nickel(II) chloride hexahydrate ($NiCl_2{\cdot}6H_2O$) were dissolved in 3 mL of water to form a dark red solution, followed by ultrasonic treatment for several minutes. 600 μL of the stock solution was dropped onto a 10 mm × 20 mm FTO sample, desiccated, and kept in a vacuum dryer at room temperature immediately. Afterwards, the FTO substrate was put in a quartz tube, heated to 210 °C in 20 min, and kept at this temperature for 30 min in a nitrogen atmosphere at a flow rate of 100 standard-state cubic centimeter per minute (sccm). Finally, the FTO substrate was coated by epoxy resin and a 5 mm × 5 mm square area was exposed for electrochemical measurements to precisely accurately control the area of the catalyst film. Nickel(II) chloride hexahydrate was replaced by cobalt(II) chloride hexahydrate ($CoCl_2{\cdot}6H_2O$) to synthesize cobalt tungsten sulfide, and no Nickel(II) or cobalt(II) chloride hexahydrate was used in the preparation of the unpromoted tungsten sulfide. In the comparative experiments, nickel(II) acetate tetrahydrate and cobalt(II) acetate tetrahydrate served as the Ni^{2+} and Co^{2+} sources, and hydrochloric acid was added to ammonium tetrathiotungstate at a molar ratio of 2:3 as the precursor of the unpromoted tungsten sulfide. Similar catalyst films were also deposited on the GC substrates for our electrochemical testing.

2.4. Characterization

The samples were characterized by field-emission scanning electron microscopy (FE-SEM, Hitachi S4800), high-resolution transmission electron microscopy (HR-TEM, JEOL-2100), X-ray powder diffraction (XRD, Philips, Xpert), and X-ray photoelectron spectroscopy (XPS, PHI5000 VersaProbe). Thermogravimetric analysis (TGA) and differential scanning calorimetry (DSC) were performed on a STA-449C (Netzsch Instruments) thermomicrobalance under nitrogen. The nitrogen adsorption and desorption isotherms were acquired at 77 K on a TriStar 3000 (Micromeritics Instrument Co.) adsorption analyzer and the specific surface areas were determined from nitrogen adsorption according to the Brunauer–Emmett–Teller (BET) method.

2.5. Electrochemical measurements

The electrochemical measurements were carried out using a three-electrode system on the CHI 660D workstation (CH Instrument) at ambient temperature in a 0.5 M H_2SO_4 solution. The catalyst films deposited on FTO-coated glass were used as the working electrode, whereas the Ag/AgCl (in 3.5 M KCl solution) electrode and platinum mesh served as the reference and counter electrodes, respectively. All of the potentials reported were calibrated to the reversible hydrogen electrode (RHE) using the following equation: $E(\mathrm{RHE}) = E(\mathrm{Ag/AgCl}) + 0.059\,\mathrm{V} \times \mathrm{pH} + 0.205\,\mathrm{V}$. Polarization curves and Tafel analysis acquired from the catalyst films in 0.5 M H_2SO_4 at a scanning rate of 2 mV s^{-1}. Electrochemical impedance spectroscopy (EIS) measurements were performed using the same configuration at −0.10 V vs. RHE from 10^5 to 0.1 Hz with an AC voltage of 5 mV. The impedance experiments were conducted to determine the series resistance and subsequent correct the Tafel analysis for iR losses. In the galvanostatic polarization experiment, the headspace of the cathodic compartment was purged with high purity nitrogen for 2 h with vigorous stirring before the measurement. The evolved hydrogen was quantified by a GC-8A (Shimadzu Co., Ar carrier gas) gas chromatograph.

3. Results and discussion

MS_4^{2-} anions have been extensively investigated from the perspective of bioinorganic and complex chemistry [48,54]. Meanwhile thermolysis of the ammonium salts ($(NH_4)_2MS_4$) is widely employed to fabricate 2H-MS_2 as HDS catalysts [52,55]. The catalysts reported here are produced on FTO by simple thermal decomposition using ammonium tetrathiotungstate ($(NH_4)_2WS_4$), nickel(II) chloride, and cobalt(II) chloride as precursors. Some catalysts are deposited on glassy carbon (GC) substrates for comparison. By heating $(NH_4)_2WS_4$, amorphous WS_x is produced between 170 and 310 °C. When the temperature is above 350 °C, $(NH_4)_2WS_4$ begins to decompose into crystalline 2H-WS_2 (Fig. S1).

The undoped tungsten sulfide annealed at 210 °C displays a branched texture with a typical dimension of several micrometers (Fig. S2a–c). In contrast, as shown in Fig. 1a and b, the nickel doped film exhibits a uniform nanoporous morphology with characteristic dimensions of 50–300 nm with a thickness of about 18 μm (Fig. S3). The cobalt tungsten sulfide is also porous but has more cracks (Fig. S2d–f). The absence of lattice fringes in the HR-TEM images and typical diffraction pattern in SAED reveal that the catalyst films produced at 210 °C are amorphous (Fig. 1c and d; Fig. S4a–f). The elemental mapping shown in Fig. 1e indicates that Ni, W, and S

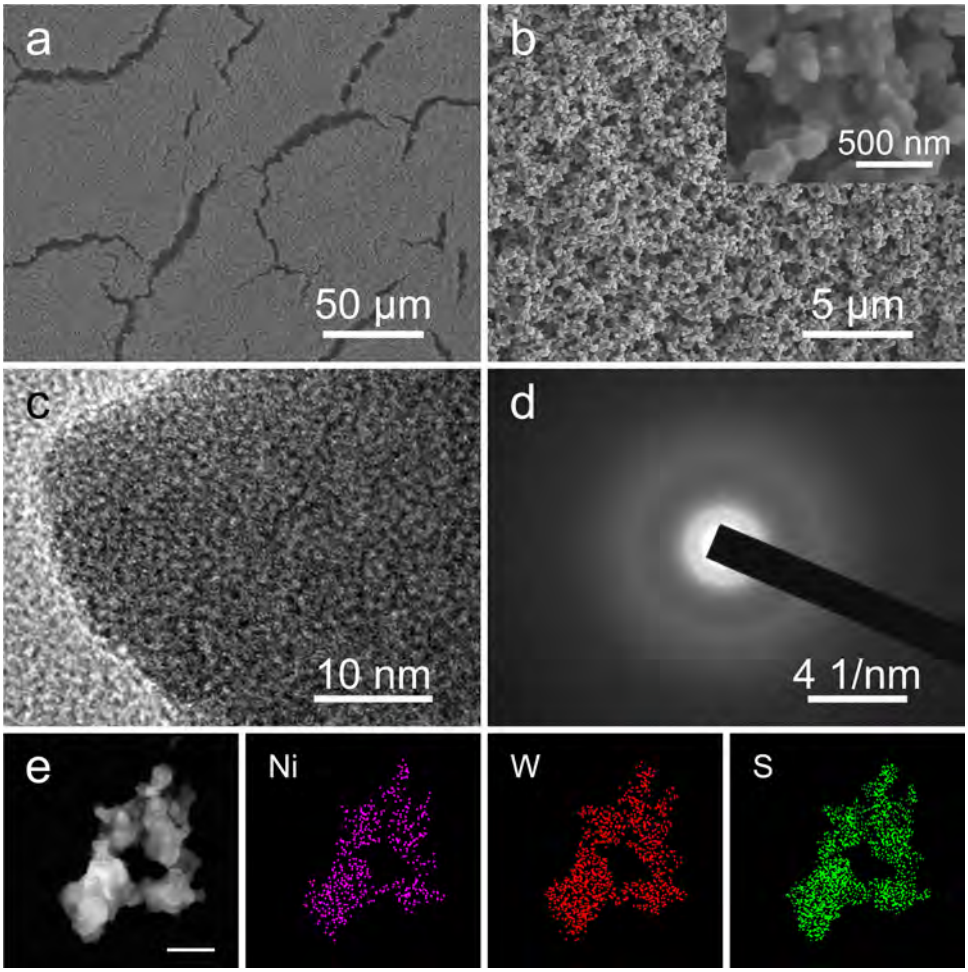

Fig. 1. (a and b) FE-SEM images of the nickel tungsten sulfide film prepared by thermolysis at 210 °C on FTO with the inset in (b) depicting the magnified local image, (c) high-resolution TEM image, (d) SAED pattern of a nickel tungsten sulfide nanoparticle exhibiting amorphous structure, and (e) elemental maps of the nanoparticle revealing the homogeneous distribution of Ni, W, and S (scale bar = 100 nm).

are homogeneously distributed (Fig. S5). The amorphous nature is further confirmed by the broad XRD peaks (Fig. S6) [55]. When the annealing temperature reaches 400 °C, the morphology of catalysts changes slightly. Both samples show polycrystalline 2H-WS_2 XRD patterns. No crystalline nickel sulfide side-phase like Ni_3S_2 is observed from nickel tungsten sulfide, indicating that the catalyst processed at 400 °C is a single NiWS phase, corroborated by TEM and SAED (Figs. S2g–l, S4g–l and S6).

To investigate the electrocatalytic activity of the samples, linear sweep voltammetry is performed in 0.5 M H_2SO_4 at 2 mV s^{-1}. Fig. 2a shows the polarization curves of the a-WS_x prepared at 210 °C with different Ni concentrations. The HER efficiency reaches a maximum when the Ni to W ratio is 1:3. The non-baseline current cannot be observed from the a-WS_x before a 300 mV overpotential, but the optimal NiWS structure with optimal loading shows an onset potential of ~100 mV and a current density of 14.1 mA cm^{-2} at −0.30 V vs. RHE (Fig. S7). Fig. 2b illustrates the influence of the annealing temperature on the HER performance of NiWS (Ni:W = 1:3). According to the above analysis, NiWS is amorphous at below 300 °C and polycrystalline over 350 °C. The HER activity shows an 'N' shape relationship with annealing temperature. The amorphous NiWS (a-NiWS) processed at 210 °C exhibits the highest activity and a minimal efficiency is observed at 240 °C. In contrast, poor HER efficiency is observed from the undoped catalysts produced in the same temperature range, as shown in Fig. S8. This unusual temperature dependence of the HER activity observed from NiWS is quite different from that of MoS_2 nanosheets [56] and amorphous MoS_x [40].

After replacing Ni^{2+} with Co^{2+}, the catalyst film again unambiguously shows enhanced activity at an onset potential of ~120 mV (Fig. S9). Consistent with the best amorphous NiWS structure, the Co to W ratio is 1:3 and the catalyst is treated at 210 °C. To achieve a current density of 10 mA cm^{-2}, overpotentials of 604, 330, and 265 mV are required for the amorphous WS_x, CoWS, and NiWS films, respectively. A drastic decrease of 339 mV is observed from NiWS compared to a-WS_x. Herein, the effect of Ni is much more pronounced than previously reported Ni-promoted MoS_2 microspheres [57], Co-doped 2H-MS_2 [5], and Fe/Co/Ni-promoted amorphous MoS_3 [49]. This activity enhancement is further confirmed by using nickel(II) acetate and cobalt(II) acetate as the Ni^{2+} and Co^{2+} sources (Fig. S10). After correcting for the ohmic potential drop (iR) loss, rather small overpotentials of 189 and 250 mV are needed to deliver a current density of 10 mA cm^{-2} for the Ni and Co doped catalysts, respectively (Figs. S9 and S11).

With regard to the amorphous NiWS annealed below 180 °C and CoWS annealed at 210 °C, a reduction peak emerges prior to hydrogen evolution in the first polarization scan and disappears from the second scan (Fig. S12). The reduction peak of NiWS becomes smaller as the annealing temperature increases from 160 to 180 °C and completely vanishes from the film annealed at 210 °C. The reduction process is also observed from electro-polymerized amorphous MoS_x [38] and crystalline Cu_2MoS_4 [53]. In the XPS spectra

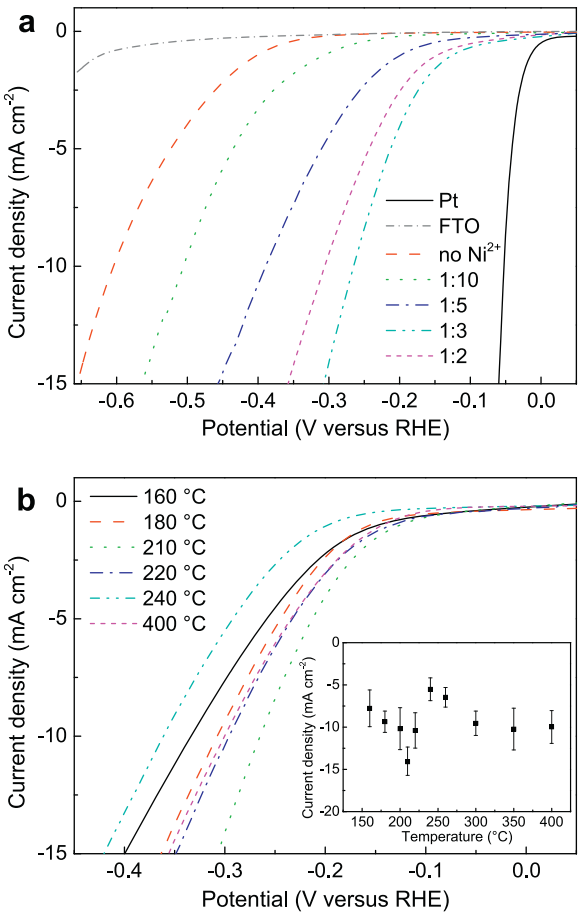

Fig. 2. Polarization curves acquired from the catalyst films on FTO in 0.5 M H_2SO_4 at a scanning rate of 2 mV s^{-1}. (a) Unpromoted and nickel promoted catalyst films annealed at 210 °C (Ni to W ratio varying from 1:10 to 1:2). The corresponding curve of a Pt foil is shown for comparison. (b) Nickel tungsten sulfide films annealed at different temperature. Curves of 160 and 180 °C are from the second polarization scans which show a reduction process in the first scan. The inset in (b) depicts the corresponding current density at −0.30 V vs. RHE as a function of temperature. The error bars are based on several measurements on multiple samples.

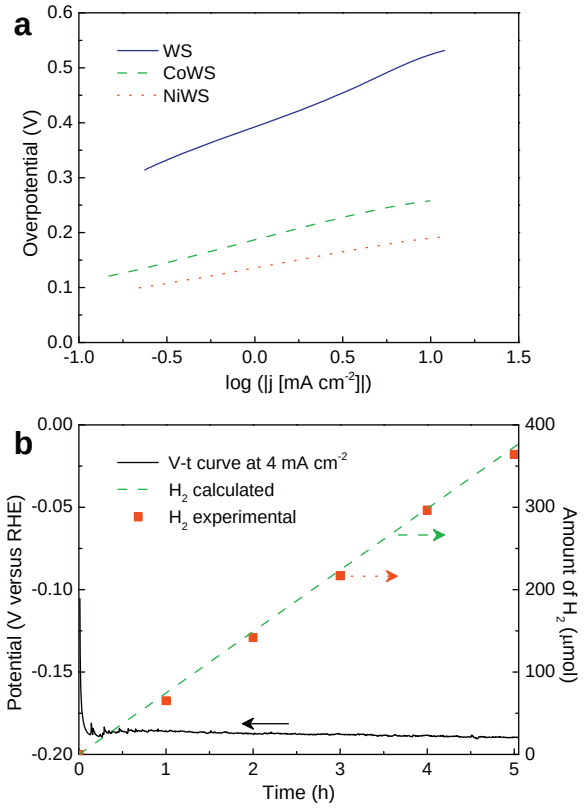

Fig. 3. (a) Tafel plots of unpromoted, nickel and cobalt promoted amorphous tungsten sulfide films (WS, NiWS, and CoWS). (b) Galvanostatic polarization curve (black line) showing the potential required to reach a 4 mA cm^{-2} current for the amorphous NiWS film on FTO. Corresponding theoretically derived hydrogen evolution (green dashed line) assuming a 100% Faraday yield with the H_2 production measured by gas chromatography (red square dots) as a function of time. (For interpretation of the references to color in this figure legend, the reader is referred to the web version of this article.)

(Fig. S13), distinct reduction of S_2^{2-} to S^{2-} is observed from the first polarization scan acquired from the NiWS annealed at 180 °C and CoWS at 210 °C. This also reflects the reduction process [38].

The Tafel plots in Fig. 3a provide insights into the mechanism [10]. After iR correction, the linear segments are fitted to the Tafel equation ($\eta = a + b\log|j|$) to obtain the exchange current density (j_0) and Tafel slope (b) [59]. Exchange current densities of 0.86, 3.2, and 3.5 μA cm^{-2} are obtained from the undoped as well as cobalt and nickel incorporated catalyst films, respectively. The WS_x exhibits a large Tafel slope of 129 mV per decade, indicating that the discharge process is slow and rate-determining (see Tafel analysis in Supporting Information) [12]. A Tafel slope of 55 mV per decade observed from the amorphous NiWS film reveals the Volmer–Heyrovsky mechanism and the rate limiting step is the electrochemical desorption reaction [13]. Hence, it is likely that Ni reduces the free energy barrier in the discharge reaction to at least that of the following desorption reaction resulting in the obvious decrease in the Tafel slope [6]. Besides, a more complex HER mechanism is suggested for amorphous CoWS with a higher Tafel slope of 74 mV per decade. This Tafel slope cannot be simply ascribed to a purely activation controlled dynamic process [58]. The Ni/Co doped catalysts with enhanced HER kinetics have enormous potential in water-splitting devices [60].

Galvanostatic polarization is performed to determine the stability of the amorphous NiWS (Fig. 3b) [61]. An overpotential of 188 mV is required to reach a current density of 4 mA cm^{-2} with slight degradation during the 5 h span. The amount of evolved hydrogen determined by gas chromatography demonstrates unity Faradaic efficiency. The durability is further confirmed by constant-voltage electrolysis at 250 mV overpotential showing a current density of 8.6 mA cm^{-2} for 24 h (Fig. S14a). The fluctuation in the cathodic current may originate from damage in the catalyst film caused by the hydrogen bubbles (Fig. S15) [62]. Moreover, our durability test of 24 h reveals robustness of the catalyst materials left in air for a month (Fig. S14b).

In catalysis, the turnover frequency (TOF) of each active site is commonly employed to evaluate the intrinsic activity [11]. Assuming that all the surface sites are catalytically active, we can estimate the TOF values (see Figs. S16 and S17 and TOF calculation in Supporting Information) [16]. The calculated TOFs of the H_2 molecules are 0.34 and 0.12 s^{-1} at 300 mV overpotential for amorphous NiWS and CoWS. These values are close to those of other efficient molybdenum sulfide catalysts [39] but smaller than those of the accurately accounted MoS_2 edge sites [22] or molecular mimic catalyst [63]. As the active sites may occupy only a small fraction of the surface, the actual TOF may be even larger [39].

Although the amorphous NiWS is comparable to other non-precious HER catalysts, its electrocatalytic property is still inferior to that of Pt. Pt(1 1 1) exhibits a Tafel slope of 29 mV dec^{-1}, exchange current density of 450 μA cm^{-2}, and TOF of 0.9 s^{-1} [22]. The performance gap is probably due to the intrinsically low

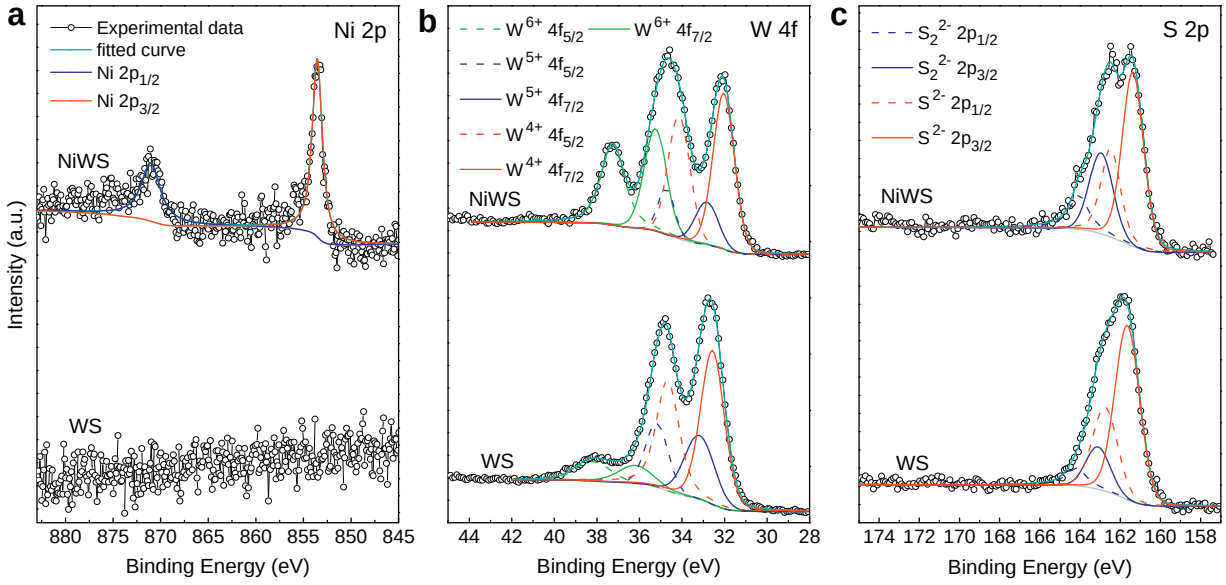

Fig. 4. XPS spectra obtained from amorphous nickel tungsten sulfide (NiWS) and amorphous tungsten sulfide (WS): (a) Ni 2p, (b) W 4f, and (c) S 2p. The black circle line represents the experimental data and the cyan line is the fitted curve (Fig. S19).

electrical conductivity of the amorphous films and poor synergistic effects between the catalyst and substrate [64]. This is similar to the case of amorphous molybdenum sulfide. The activity of the MoS_x/NCNT (N-doped carbon nanotube) hybrid is superior to that of the electro-deposited MoS_x film [38,64], but surprisingly, the MoS_x/PPy (polypyrrole) copolymer displays even much higher efficiency comparable to that of commercial Pt/C catalysts [62]. Hence, more work is needed to elucidate the HER mechanism and improve the activity [65]. In addition, we have evaluated the performance of the catalyst films on the GC electrode (Fig. S18). Remarkable increase in the exchange current density is observed as demonstrated by values of 17.4 and 13.4 $\mu A\,cm^{-2}$ observed from the amorphous NiWS and CoWS, respectively. Here, we would like to mention that better performance can be expected by coupling with conductive electrode like graphene [59].

To obtain more knowledge about the chemical nature of the catalysts, XPS is performed to determine the atomic composition and bonding states. As shown in Fig. 4, the Ni 2p spectrum of the NiWS film annealed at 210 °C shows two peaks corresponding to the Ni $2p_{1/2}$ and $2p_{3/2}$ (see the XPS results of amorphous CoWS in Supporting Information, Figs. S20 and S21) [66]. The Ni $2p_{3/2}$ peak at 853.54 eV is attributed to the Ni 2p in NiWS phase as it differs from the typical Ni $2p_{3/2}$ signal from Ni_3S_2 at 853.0 eV [51,66]. The W 4f spectra are fitted to several doublets including W^{4+} $4f_{5/2-7/2}$, W^{5+} $4f_{5/2-7/2}$, and W^{6+} $4f_{5/2-7/2}$ [44]. Signals of W^{4+} and W^{5+} species are commonly observed from amorphous WS_x and its derivatives [67], but the ratios of the contents are smaller in amorphous NiWS than crystalline WS_x. The W^{6+} peaks representing oxidation of W are more obvious in NiWS, as the precursor becomes more unstable after WS_4^{2-} interacts with Ni^{2+} [48,67]. In the S 2p spectrum, the peaks at 162.47–162.75 and 161.37–161.65 eV correspond to the S $2p_{1/2}$ and $2p_{3/2}$ of S^{2-} ligand [38]. Previous studies have revealed that the S_2^{2-} ligand may play an important role in the HER activity of amorphous MoS_x [40,62]. In NiWS, the intensity of the S $2p_{1/2}$ and $2p_{3/2}$ peaks at 164.05–164.20 and 162.95–163.10 eV, which indicate the presence of bridging S_2^{2-} and/or apical S^{2-} [62], is larger than that in WS_x. By integrating the XPS data, the amorphous NiWS structure is derived to be $Ni_{0.36}WS_{2.78}$.

With regard to the amorphous NiWS after the HER studies, the W^{6+} signal increases slightly, while the S_2^{2-} content decreases slightly (Figs. S22 and S23). We have also acquired XPS spectra from the NiWS annealed at 180 and 240 °C (Figs. S24–S26). Notable difference is from the W 4f and S 2p regions compared to the NiWS annealed at 210 °C, especially the signal of S_2^{2-} decreases with increasing annealing temperature. For the NiWS annealed at 400 °C, the Ni 2p spectrum is similar to that from the NiWS annealed at 210 °C. However, in the W 4f and S 2p regions, both the undoped and nickel incorporated catalysts show similar features as 2H-WS_2 (Figs. S28 and S29) [27,52]. XPS indicates that the proper Ni:W:S ratio and concomitant binding structures formed at 210 °C are responsible for the excellent catalytic activity.

Similar to other effective HER catalysts like Pt, the edge sites on 2H-MS_2 has a free energy of hydrogen adsorption (ΔG_H) close to zero, suggesting that the uncoordinated centers are crucial [22,54]. Theoretical and experimental studies have revealed that molybdenum sulfide and tungsten sulfide with various coordination states such as MoS_2 edge, MoS_4^{2-}, $Mo_3S_4^{4+}$, and $Mo_3S_{13}^{2-}$ exhibit different ΔG_H and catalytic ability [68–71]. Ni and Co are widely applied to MS_2-derived HER or HDS catalysts because of the enhancement effect rendered by the edge structures [5,46]. For 2H-WS_2, ΔG_H of the S-edge decreases from 0.22 to 0.07 eV after cobalt incorporation [5].

Amorphous materials offer more diversity and flexibility from the perspective of composition and microstructure than the crystalline counterparts and it is possible to tailor the surface chemistry of amorphous materials to improve the activity on the molecular level [36,37]. In MS_4^{2-}, Mo or W is tetrahedrally coordinated to S with the T_d symmetry and considerable π-bonding proportion exists in the metal–sulfur (M–S) bonds, especially for WS_4^{2-}. Owing to the smaller electron density on the S atoms, the proton affinity of WS_4^{2-} is lower than that of MoS_4^{2-} [48]. The MS_4^{2-} ion with low-lying unoccupied orbitals shows versatile coordination behavior with Ni^{2+} or Co^{2+} forming complexes like $[M'(MS_4)_2]^{n-}$ or $M'MS_4$ [49–52]. In these complexes, the strong 3d–π interactions in the ligand orbitals (i.e. $M' \rightarrow MS_4$ electron delocalization) occur, accompanied by reduction in the coordination symmetry and perturbation of the electronic structure. The bonding states of the square planar coordinated Ni in the complexes differ from those of tetrahedrally coordinated Co [48]. Meanwhile, the structure of amorphous tungsten sulfide can be altered by thermal treatment. Different from both WS_4^{2-} and 2H-WS_2, a chain-model with a W_2S_9 unit is proposed to be the typical structure of WS_x in which the W atoms may

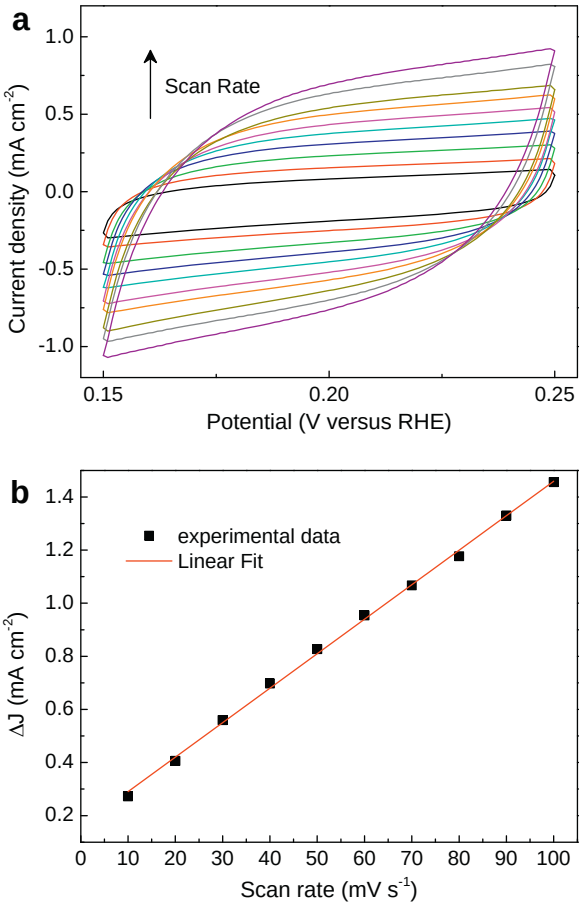

Fig. 5. (a) Cyclic voltammograms of amorphous NiWS measured at different scanning rates (10–100 mV s^{-1}) in 0.5 M H_2SO_4. (b) Corresponding scanning rate dependence of the current density at 0.20 V vs. RHE. The slope of the ΔJ vs. scanning rate curve is twice the capacitance. C_{dl} of amorphous NiWS is 6500 μF cm^{-2}.

have oxidation state IV or V and the W_2 dimer is bridged to S^{2-} and S_2^{2-} [55]. Hence, Ni/Co introduction and heating treatment are utilized together to optimize the amorphous structure in an attempt to enhance the HER activity and as a result, the chemical structure is altered significantly as disclosed by the XPS spectra.

To further elucidate the effects of Ni or Co incorporation, the electrochemically active surface area (S_{echem}) is assessed by capacitance measurements (Fig. 5) because S_{echem} is assumed to be linearly proportional to the double layer capacitance (C_{dl}) [39,49]. The relative value (S^*_{echem}) of S_{echem} can be obtained by normalization of C_{dl} and the relative geometric surface area (S^*_{geom}) is derived from the BET data (Figs. S29–S32). It is generally supposed that S_{echem} is directly proportional to the amount of active sites in HER [39]. After doping, S^*_{echem} becomes larger compared to the relatively small increase in S^*_{geom} (Table 1). In addition, for amorphous NiWS, the values of S^*_{echem} at 180 and 240 °C are smaller than that at 210 °C, but still much larger than those of a-WS_x. The relative surface density of the active sites (σ_{eff}) can be determined by dividing S^*_{echem} by S^*_{geom} Compared to WS_x, the σ_{eff} values of amorphous NiWS and CoWS are 263 and 124 times larger, respectively, indicating pronounced increase in the active site density due to incorporation of Ni or Co.

Table 1
HER performance and relative surface density of active sites (σ_{eff}) of the amorphous WS_x, CoWS, and NiWS films. b: Tafel slope, j_0: exchange current density, S^*_{geom} and S^*_{echem} referring to the relative geometric and electrochemical active surface areas, respectively.

Material	b (mV dec^{-1})	j_o (μA cm^{-1})	S^*_{geom}	S^*_{echem}	σ_{eff}
WS_x	129	0.86	1	1	1
CoWS	74	3.2	1.89	234	124
NiWS	55	3.5	1.30	342	263

In contrast to the Co/Ni–S centers in the crystalline $CoWS_x$ and $NiWS_x$ [43], it is more likely that the enhanced activity arises from the structure of Ni–W–S or Co–W–S, as the performance of the catalysts is not directly related to the Ni/Co concentration [49]. Dopant atoms and thermal treatment greatly alter the electronic structures, especially the coordination states, and so ΔG_H can be tuned [5]. Under optimal conditions, the average ΔG_H is expected to be largely reduced and inert surface sites are galore activated based on the previously theoretical analyses [5,49]. Therefore, the active site density is increased, especially in amorphous NiWS annealed at 210 °C. The discharge reaction barrier is reduced by reformative bonding of the intermediates and closer proximity among active sites [70]. Consequently, the electrochemical desorption reaction becomes more rate determining and the HER dynamics is accelerated [6,70]. Hence, the intrinsic activity in amorphous NiWS and CoWS is significantly improved and comparable to that of other MX_2-based catalysts (Table S1).

4. Conclusion

In conclusion, amorphous nickel/cobalt tungsten sulfide is synthesized by a thermolysis and the catalysts, especially amorphous NiWS, deliver outstanding catalytic performance. Hence, utilization of tungsten sulfide derived materials in HER catalysis is no longer limited to the crystalline 2H or 1T phase. Ni/Co incorporation and thermal treatment alter the morphology and chemical structure of the amorphous WS_x and produce numerous surface sites. By adopting the optimal conditions, the density of active surface sites is significantly increased and the HER kinetics is largely promoted compared to WS_x. The results clearly indicate that amorphous NiWS and CoWS catalysts have immense potentials in water splitting devices.

Acknowledgements

This work was supported by National Basic Research Programs of China under Grants Nos. 2011CB922102 and 2014CB339800 and National Natural Science Foundation (Nos. 61264008 and 11374141). Partial support was also from Guangdong – Hong Kong Technology Cooperation Funding Scheme (TCFS) GHP/015/12SZ.

Appendix A. Supplementary data

Supplementary data associated with this article can be found, in the online version, at http://dx.doi.org/10.1016/j.apsusc.2015.03.018.

References

[1] S. Cobo, J. Heidkamp, P.A. Jacques, J. Fize, V. Fourmond, L. Guetaz, B. Jousselme, V. Ivanova, H. Dau, S. Palacin, et al., A Janus cobalt-based catalytic material for electro-splitting of water, Nat. Mater. 11 (2012) 802–807.
[2] A. Kudo, Y. Miseki, Heterogeneous photocatalyst materials for water splitting, Chem. Soc. Rev. 38 (2009) 253–278.
[3] M.G. Walter, E.L. Warren, J.R. Mckone, S.W. Boettcher, Q.X. Mi, E.A. Santori, N.S. Lewis, Solar water splitting cells, Chem. Rev. 110 (2010) 6446–6473.
[4] M. Chhowalla, H.S. Shin, G. Eda, L.J. Li, K.P. Loh, H. Zhang, The chemistry of two-dimensional layered transition metal dichalcogenide nanosheets, Nat. Chem. 5 (2013) 263–275.
[5] J. Bonde, P.G. Moses, T.F. Jaramillo, J.K. Nørskov, I. Chorkendorff, Hydrogen evolution on nano-particulate transition metal sulfides, Faraday Discuss. 140 (2008) 219–231.
[6] H.T. Wang, D.S. Kong, P. Johanes, J.J. Cha, G.Y. Zheng, K. Yan, N. Liu, Y. Cui, $MoSe_2$ and WSe_2 nanofilms with vertically aligned molecular layers on curved and rough surfaces, Nano Lett. 13 (2013) 3426–3433.

[7] F.H. Saadi, A.I. Carim, J.M. Velazquez, J.H. Baricuatro, C.C.L. McCrory, M.P. Soriaga, N.S. Lewis, Operando synthesis of macroporous molybdenum diselenide films for electrocatalysis of the hydrogen-evolution reaction, ACS Catal. 4 (2014) 2866–2873.

[8] L. Liao, J. Zhu, X.J. Bian, L.N. Zhu, M.D. Scanlon, H.H. Girault, B.H. Liu, MoS_2 formed on mesoporous graphene as a highly active catalyst for hydrogen evolution, Adv. Funct. Mater. 23 (2013) 5326–5333.

[9] B. Hinnemann, P.G. Moses, J. Bonde, K.P. Jørgensen, J.H. Nielsen, S. Horch, I. Chorkendorff, J.K. Nørskov, Biomimetic hydrogen evolution: MoS_2 nanoparticles as catalyst for hydrogen evolution, J. Am. Chem. Soc. 127 (2005) 5308–5309.

[10] C.G. Morales-Guio, L.A. Stern, X.L. Hu, Nanostructured hydrotreating catalysts for electrochemical hydrogen evolution, Chem. Soc. Rev. 43 (2014) 6555–6569.

[11] G.J. Kubas, Fundamentals of H_2 binding and reactivity on transition metals underlying hydrogenase function and H_2 production and storage, Chem. Rev. 107 (2007) 4152–4205.

[12] L. Liao, S.N. Wang, J.J. Xiao, X.J. Bian, Y.H. Zhang, M.D. Scanlon, X.L. Hu, Y. Tang, B.H. Liu, H.H. Girault, A nanoporous molybdenum carbide nanowire as an electrocatalyst for hydrogen evolution reaction, Energy Environ. Sci. 7 (2014) 387–392.

[13] W.F. Chen, S. Iyer, S. Iyer, K. Sasaki, C.H. Wang, Y. Zhu, J.T. Muckerman, E. Fujita, Biomass-derived electrocatalytic composites for hydrogen evolution, Energy Environ. Sci. 6 (2013) 1818–1826.

[14] A.T. Garcia-Esparza, D. Cha, Y.W. Ou, J. Kubota, K. Domen, K. Takanabe, Tungsten carbide nanoparticles as efficient cocatalysts for photocatalytic overall water splitting, ChemSusChem 6 (2013) 168–181.

[15] Y. Zhao, K. Kamiya, K. Hashimoto, S. Nakanishi, Hydrogen evolution by tungsten carbonitride nanoelectrocatalysts synthesized by the formation of a tungsten acid/polymer hybrid in situ, Angew. Chem. Int. Ed. 52 (2013) 13638–13641.

[16] E.J. Popczun, J.R. McKone, C.G. Read, A.J. Biacchi, A.M. Wiltrout, N.S. Lewis, R.E. Schaak, Nanostructured nickel phosphide as an electrocatalyst for the hydrogen evolution reaction, J. Am. Chem. Soc. 135 (2013) 9267–9270.

[17] X. Li, J.G. Yu, J.X. Low, Y.P. Fang, J. Xiao, X.B. Chen, Engineering heterogeneous semiconductors for solar water splitting, J. Mater. Chem. A 3 (2015) 2485–2534.

[18] J.R. Ran, J. Zhang, J.G. Yu, M. Jaroniec, S.Z. Qiao, Earth-abundant cocatalysts for semiconductor-based photocatalytic water splitting, Chem. Soc. Rev. 43 (2014) 7787–7812.

[19] J.H. Yang, D.G. Wang, H.X. Han, C. Li, Roles of cocatalysts in photocatalysis and photoelectrocatalysis, Acc. Chem. Res. 46 (2013) 1900–1909.

[20] S.W. Cao, Y.P. Yuan, J. Barber, S.C.J. Loo, C. Xue, Noble-metal-free g-C_3N_4/Ni(dmgH)$_2$ composite for efficient photocatalytic hydrogen evolution under visible light irradiation, Appl. Surf. Sci. 319 (2014) 344–349.

[21] J. Zhang, L.F. Qi, J.R. Ran, J.G. Yu, S.Z. Qiao, Ternary NiS/$Zn_xCd_{1-x}S$/reduced graphene oxide nanocomposites for enhanced solar photocatalytic H_2-production activity, Adv. Energy Mater. 4 (2014) 1301925.

[22] T.F. Jaramillo, K.P. Jørgensen, J. Bonde, J.H. Nielsen, S. Horch, I. Chorkendorff, Identification of active edge sites for electrochemical H_2 evolution from MoS_2 nanocatalysts, Science 317 (2007) 100–102.

[23] M.A. Lukowski, A.S. Daniel, F. Meng, A. Forticaux, L.S. Li, S. Jin, Enhanced hydrogen evolution catalysis from chemically exfoliated metallic MoS_2 nanosheets, J. Am. Chem. Soc. 135 (2013) 10274–10277.

[24] D. Voiry, M. Salehi, R. Silva, T. Fujita, M.W. Chen, T. Asefa, V.B. Shenoy, G. Eda, M. Chhowalla, Conducting MoS_2 nanosheets as catalysts for hydrogen evolution reaction, Nano Lett. 13 (2013) 6222–6227.

[25] J. Kibsgaard, Z. Chen, B.N. Reinecke, T.F. Jaramillo, Engineering the surface structure of MoS_2 to preferentially expose active edge sites for electrocatalysis, Nat. Mater. 11 (2012) 963–969.

[26] Y.D. Hou, B.L. Abrams, P.C.K. Vesborg, M.E. Bjorketun, K. Herbst, L. Bech, A.M. Setti, C.D. Damsgaard, T. Pedersen, O. Hansen, Bioinspired molecular Co-catalysts bonded to a silicon photocathode for solar hydrogen evolution, Nat. Mater. 10 (2011) 434–438.

[27] J. Lin, Z.W. Peng, G. Wang, D. Zakhidov, E. Larios, M.J. Yacaman, J.M. Tour, Enhanced electrocatalysis for hydrogen evolution reactions from WS_2 nanoribbons, Adv. Energy Mater. 4 (2014) 1301875.

[28] Z.Z. Wu, B.Z. Fang, A. Bonakdarpour, A.K. Sun, D.P. Wilkinson, D.Z. Wang, WS_2 nanosheets as a highly efficient electrocatalyst for hydrogen evolution reaction, Appl. Catal. B 125 (2012) 59–66.

[29] C.L. Choi, J. Feng, Y.G. Li, J. Wu, A. Zak, R. Tenne, H.J. Dai, WS_2 nanoflakes from nanotubes for electrocatalysis, Nano Res. 6 (2013) 921–928.

[30] L. Cheng, W.J. Huang, Q.F. Gong, C.H. Liu, Z. Liu, Y.G. Li, H.J. Dai, Ultrathin WS_2 nanoflakes as a high-performance electrocatalyst for the hydrogen evolution reaction, Angew. Chem. Int. Ed. 53 (2014) 7860–7863.

[31] J. Kim, S. Byun, A.J. Smith, J. Yu, J.X. Huang, Enhanced electrocatalytic properties of transition-metal dichalcogenides sheets by spontaneous gold nanoparticle decoration, J. Phys. Chem. Lett. 4 (2013) 1227–1232.

[32] J. Yang, D. Voiry, S.J. Ahn, D. Kang, A.Y. Kim, M. Chhowalla, H.S. Shin, Two-dimensional hybrid nanosheets of tungsten disulfide and reduced graphene oxide as catalysts for enhanced hydrogen evolution, Angew. Chem. Int. Ed. 52 (2013) 13751–13754.

[33] Z.H. Pu, Q. Liu, A.M. Asiri, A.Y. Obaid, X.P. Sun, One-step electrodeposition fabrication of graphene film-confined WS_2 nanoparticles with enhanced electrochemical catalytic activity for hydrogen evolution, Electrochim. Acta 134 (2014) 8–12.

[34] D. Voiry, H. Yamaguchi, J.W. Li, R. Silva, D.C.B. Alves, T. Fujita, M.W. Chen, T. Asefa, V.B. Shenoy, G. Eda, et al., Enhanced catalytic activity in strained chemically exfoliated WS_2 nanosheets for hydrogen evolution, Nat. Mater. 12 (2013) 850–855.

[35] M.A. Lukowski, A.S. Daniel, C.R. English, F. Meng, A. Forticaux, R.J. Hamers, S. Jin, Highly active hydrogen evolution catalysis from metallic WS_2 nanosheets, Energy Environ. Sci. 7 (2014) 2608–2613.

[36] M.W. Kanan, D.G. Nocera, In situ formation of an oxygen-evolving catalyst in neutral water containing phosphate and Co^{2+}, Science 321 (2008) 1072–1075.

[37] J.F. Deng, H.X. Li, W.J. Wang, Progress in design of new amorphous alloy catalysts, Catal. Today 51 (1999) 113–125.

[38] D. Merki, S. Fierro, H. Vrubel, X.L. Hu, Amorphous molybdenum sulfide films as catalysts for electrochemical hydrogen production in water, Chem. Sci. 2 (2011) 1262–1267.

[39] J.D. Benck, Z.B. Chen, L.Y. Kuritzky, A.J. Forman, T.F. Jaramillo, Amorphous molybdenum sulfide catalysts for electrochemical hydrogen production: insights into the origin of their catalytic activity, ACS Catal. 2 (2012) 1916–1923.

[40] Y.H. Chang, C.T. Lin, T.Y. Chen, C.L. Hsu, Y.H. Lee, W.J. Zhang, K.H. Wei, L.J. Li, Highly efficient electrocatalytic hydrogen production by MoS_x grown on graphene-protected 3D Ni foams, Adv. Mater. 25 (2013) 756–760.

[41] H. Vrubel, D. Merki, X.L. Hu, Hydrogen evolution catalyzed by MoS_3 and MoS_2 particles, Energy Environ. Sci. 5 (2012) 6136–6144.

[42] T.Y. Wang, L. Liu, Z.W. Zhu, P. Papakonstantinou, J.B. Hu, H.Y. Liu, M.X. Li, Enhanced electrocatalytic activity for hydrogen evolution reaction from self-assembled monodispersed molybdenum sulfide nanoparticles on an Au electrode, Energy Environ. Sci. 6 (2013) 625–633.

[43] P.D. Tran, S.Y. Chiam, P.P. Boix, Y. Ren, S.S. Pramana, J. Fize, V. Artero, J. Barber, Novel cobalt/nickel–tungsten–sulfide catalysts for electrocatalytic hydrogen generation from water, Energy Environ. Sci. 6 (2013) 2452–2459.

[44] T.Y. Chen, Y.H. Chang, C.L. Hsu, K.H. Wei, C.Y. Chiang, L.J. Li, Comparative study on MoS_2 and WS_2 for electrocatalytic water splitting, Int. J. Hydrogen Energy 38 (2013) 12302–12309.

[45] Z.P. Huang, C.F. Wang, Z.B. Chen, H. Meng, C.C. Lv, Z.Z. Chen, R.Q. Han, C. Zhang, Tungsten sulfide enhancing solar-driven hydrogen production from silicon nanowires, ACS Appl. Mater. Interfaces 6 (2014) 10408–10414.

[46] Y.Y. Zhu, Q.M. Ramasse, M. Brorson, P.G. Moses, L.P. Hansen, C.F. Kisielowski, S. Helveg, Visualizing the stoichiometry of industrial-style Co–Mo–S catalysts with single-atom sensitivity, Angew. Chem. Int. Ed. 53 (2014) 10723.

[47] A. Sobczynski, A.J. Bard, A. Campion, M.A. Fox, T.E. Mallouk, S.E. Webber, J.M. White, Catalytic hydrogen evolution properties of nickel-doped tungsten disulfide, J. Phys. Chem. 93 (1989) 401–403.

[48] A. Müller, E. Diemann, R. Jostes, H. Bögge, Transition metal thiometalates: properties and significance in complex and bioinorganic chemistry, Angew. Chem. Int. Ed. 20 (1981) 934–955.

[49] D. Merki, H. Vrubel, L. Rovelli, S. Fierro, X.L. Hu, Fe, Co, and Ni ions promote the catalytic activity of amorphous molybdenum sulfide films for hydrogen evolution, Chem. Sci. 3 (2012) 2515–2525.

[50] X.J. Zheng, J.H. Guo, Y.T. Shi, F.Q. Xiong, W.H. Zhang, T.L. Ma, C. Li, Low-cost and high-performance $CoMoS_4$ and $NiMoS_4$ counter electrodes for dye-sensitized solar cells, Chem. Commun. 49 (2013) 9645–9647.

[51] W. Eltzner, M. Breysse, M. Lacroix, M. Vrinat, Inorganic-chemistry approach to the preparation of sulfided mixed-phase hydrotreating catalysts using thiometalates as precursors, Polyhedron 5 (1986) 203–210.

[52] J. Espino, L. Alvarez, C. Ornelas, J.L. Rico, S. Fuentes, G. Berhault, G. Alonso, Comparative study of WS_2 and Co(Ni)/WS_2 HDS catalysts prepared by ex situ/in situ activation of ammonium thiotungstate, Catal. Lett. 90 (2003) 71–80.

[53] D.S. Kong, J.J. Cha, H.T. Wang, H.R. Lee, Y. Cui, First-row transition metal dichalcogenide catalysts for hydrogen evolution reaction, Energy Environ. Sci. 6 (2013) 3553–3558.

[54] M.L. Tang, D.C. Grauer, B. Lassalle-Kaiser, V.K. Yachandra, L. Amirav, J.R. Long, J. Yano, A.P. Alivisatos, Structural and electronic study of an amorphous MoS_3 hydrogen-generation catalyst on a quantum-controlled photosensitizer, Angew. Chem. Int. Ed. 50 (2011) 10203–10207.

[55] R.I. Walton, S.J. Hibble, A combined in situ X-ray absorption spectroscopy and X-ray diffraction study of the thermal decomposition of ammonium tetrathiotungstate, J. Mater. Chem. 9 (1999) 1347–1355.

[56] Z.Z. Wu, B.Z. Fang, Z.P. Wang, C.L. Wang, Z.H. Liu, F.Y. Liu, W. Wang, A. Alfantazi, D.Z. Wang, D.P. Wilkinson, MoS_2 nanosheets: a designed structure with high active site density for the hydrogen evolution reaction, ACS Catal. 3 (2013) 2101–2107.

[57] X.J. Lv, G.W. She, S.X. Zhou, Y.M. Li, Highly efficient electrocatalytic hydrogen production by nickel promoted molybdenum sulfide microspheres catalysts, RSC Adv. 3 (2013) 21231–21236.

[58] P.D. Tran, M. Nguyen, S.S. Pramana, A. Bhattacharjee, S.Y. Chiam, J. Fize, M.J. Field, V. Artero, L.H. Wong, J. Loo, et al., Copper molybdenum sulfide: a new efficient electrocatalyst for hydrogen production from water, Energy Environ. Sci. 5 (2012) 8912–8916.

[59] Y.G. Li, H.L. Wang, L.M. Xie, Y.Y. Liang, G.S. Hong, H.J. Dai, MoS_2 nanoparticles grown on graphene: an advanced catalyst for the hydrogen evolution reaction, J. Am. Chem. Soc. 133 (2011) 7296–7299.

[60] Q.J. Xiang, J.G. Yu, M. Jaroniec, Synergetic effect of MoS_2 and graphene as cocatalysts for enhanced photocatalytic H_2 production activity of TiO_2 nanoparticles, J. Am. Chem. Soc. 134 (2012) 6575–6578.

[61] J.F. Xie, J.J. Zhang, S. Li, F. Grote, X.D. Zhang, H. Zhang, R.X. Wang, Y. Lei, B.C. Pan, Y. Xie, Controllable disorder engineering in oxygen-incorporated MoS_2 ultrathin nanosheets for efficient hydrogen evolution, J. Am. Chem. Soc. 135 (2013) 17881–17888.

[62] T.Y. Wang, J.Q. Zhuo, K.Z. Du, B.B. Chen, Z.W. Zhu, Y.H. Shao, M.X. Li, Electrochemically fabricated polypyrrole and MoS_x copolymer films as a highly active hydrogen evolution electrocatalyst, Adv. Mater. 26 (2014) 3761–3766.

[63] H.I. Karunadasa, E. Montalvo, Y.J. Sun, M. Majda, J.R. Long, C.J. Chang, A molecular MoS_2 edge site mimic for catalytic hydrogen generation, Science 335 (2012) 698–702.
[64] D.J. Li, U.N. Maiti, J. Lim, D.S. Choi, W.J. Lee, Y. Oh, G.Y. Lee, S.O. Kim, Molybdenum sulfide/N-doped CNT forest hybrid catalysts for high-performance hydrogen evolution reaction, Nano Lett. 14 (2014) 1228–1233.
[65] X.B. Ge, L.Y. Chen, L. Zhang, Y.R. Wen, A. Hirata, M.W. Chen, Nanoporous metal enhanced catalytic activities of amorphous molybdenum sulfide for high-efficiency hydrogen production, Adv. Mater. 26 (2014) 3100–3104.
[66] L. Coulier, G. Kishan, J.A.R. van Veen, J.W. Niemantsverdriet, Influence of support-interaction on the sulfidation behavior and hydrodesulfurization activity of Al_2O_3-supported W, CoW, and NiW model catalysts, J. Phys. Chem. B 106 (2002) 5897–5906.
[67] G.F. Khudorozhko, I.P. Asanov, L.N. Mazalov, E.A. Kravtsova, G.K. Parygina, V.E. Fedorov, J.V. Mironov, The study of electronic structure of molybdenum and tungsten trisulfides and their lithium intercalates by X-ray electron and X-ray emission and absorption spectroscopy, J. Electron. Spectrosc. 68 (1994) 199–209.
[68] A. Saha, K. Raghavachari, Hydrogen evolution from water through metal sulfide reactions, J. Chem. Phys. 139 (2013) 204301.
[69] B. Wang, N. Wu, X.B. Zhang, X. Huang, Y.F. Zhang, W.K. Chen, K.N. Ding, Probing the smallest molecular model of MoS_2 catalyst: S_2 units in the $MoS_n^{-/0}$ (n = 1–5) clusters, J. Phys. Chem. A 117 (2013) 5632–5641.
[70] J. Kibsgaard, T.F. Jaramillo, F. Besenbacher, Building an appropriate active-site motif into a hydrogen-evolution catalyst with thiomolybdate $[Mo_3S_{13}]^{2-}$ clusters, Nat. Chem. 6 (2014) 248–253.
[71] S. Chatterjee, K. Sengupta, S. Dey, A. Dey, Ammonium tetrathiomolybdate: a versatile catalyst for hydrogen evolution reaction from water under ambient and hostile conditions, Inorg. Chem. 52 (2013) 14168–14177.

Supporting Information

Amorphous nickel/cobalt tungsten sulfide electrocatalysts for high-efficiency hydrogen evolution reaction

Lun Yang,[a] Xinglong Wu,[a,b,*] Xiaoshu Zhu,[c] Chengyu He,[a] Ming Meng,[a] Zhixing Gan,[a] and Paul K. Chu[d]

[a] Key Laboratory of Modern Acoustics, MOE, Institute of Acoustics and Collaborative Innovation Center of Advanced Microstructures, National Laboratory of Solid State Microstructures, Nanjing University, Nanjing 210093, P. R. China

[b] Department of Physics, NingBo University, NingBo 315001, P. R. China

[c] Center for Analysis and Testing, Nanjing Normal University, Nanjing 210093, P. R. China

[d] Department of Physics and Materials Science, City University of Hong Kong, Tat Chee Avenue, Kowloon, Hong Kong, China

Table of contents

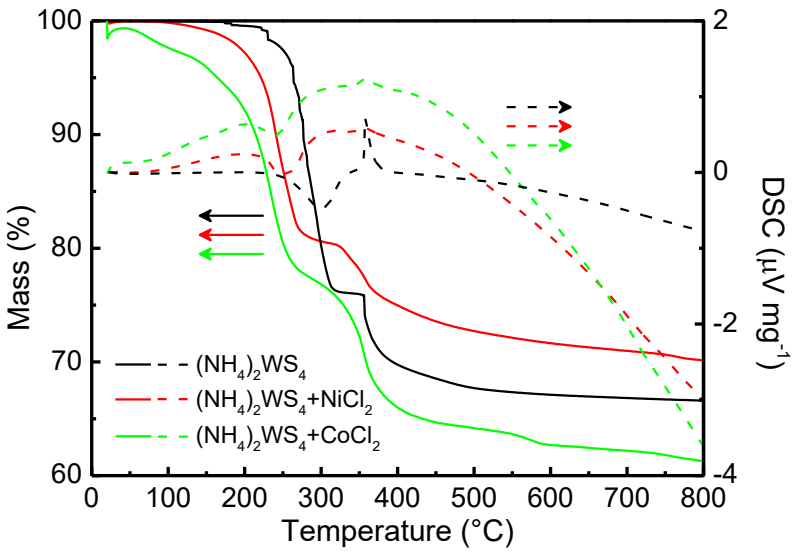

Fig. S1. TG/DSC curves of three precursors. Thermal decomposition is performed at a heating rate of 10 ^{o}C min^{-1} in nitrogen.

It is generally understood that thermal decomposition of $(NH_4)_2WS_4$ takes place by the following reactions:[S1]

$$(NH_4)_2WS_4 \rightarrow WS_3 + H_2S + 2NH_3$$

$$WS_3 \rightarrow WS_2 + S$$

Amorphous tungsten trisulfide is produced in an inert ambient at a temperature between 170 and 310 ^{o}C and the materials are stable between 310 and 350 ^{o}C. The amorphous WS_3 begins to decompose into crystalline 2H-WS_2 and S above 350 ^{o}C.[S1,S2] It is noted that decomposition of $NiCl_2$/$(NH_4)_2WS_4$ occurs at a temperature as low as 110 ^{o}C and the amorphous phase begins to crystallize at 320 ^{o}C.[S2]

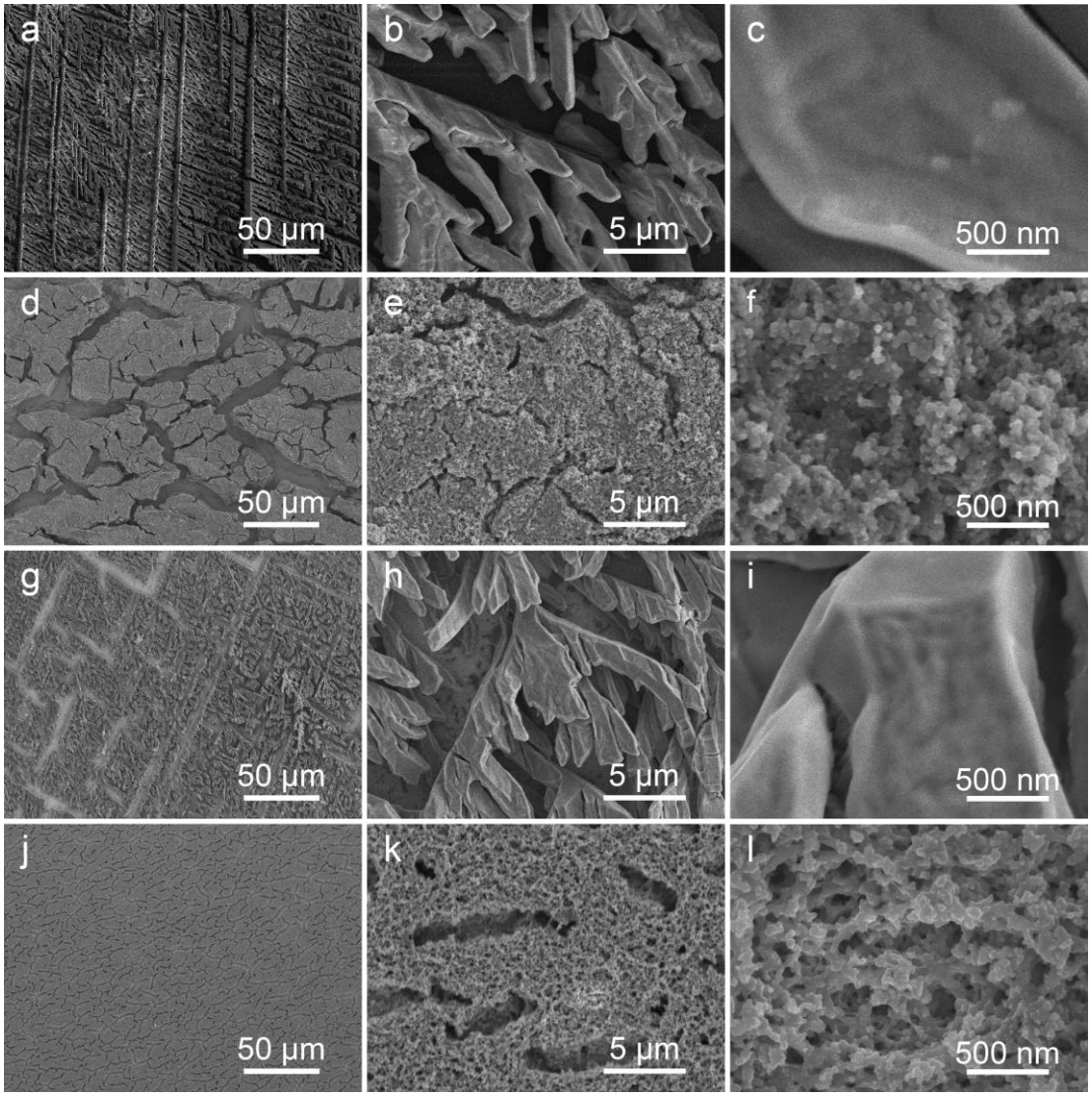

Fig. S2. FE-TEM images of the catalyst films prepared by thermolysis on FTO. (a, b, c) Tungsten sulfide film annealed at 210 ºC. (d, e, f) Cobalt tungsten sulfide film annealed at 210 ºC. (g, h, i) Tungsten sulfide film annealed at 400 ºC. (j, k, l) Nickel tungsten sulfide film annealed at 400 ºC.

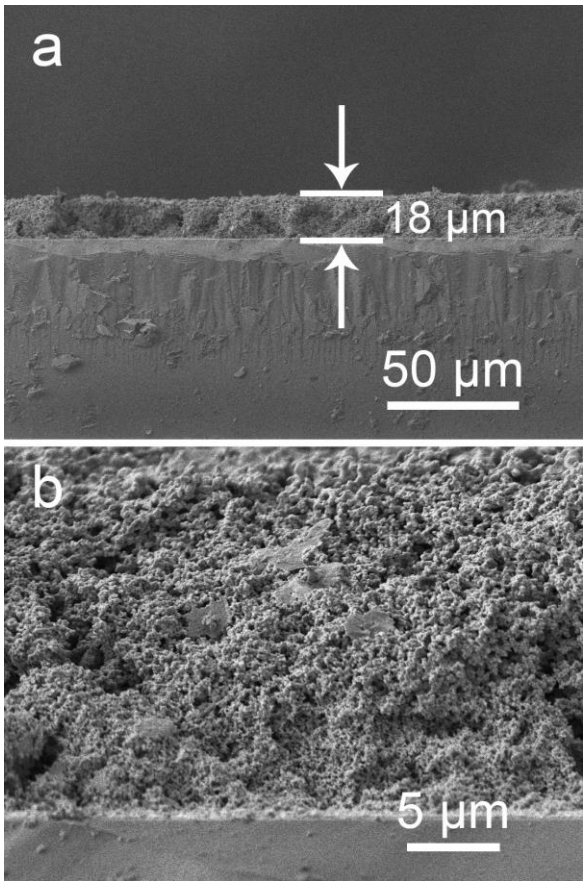

Fig. S3. (a, b) Cross-sectional FE-SEM images of the amorphous nickel tungsten sulfide film deposited on FTO electrode. The average film thickness is 18 μm (varying from 15 to 20 μm).

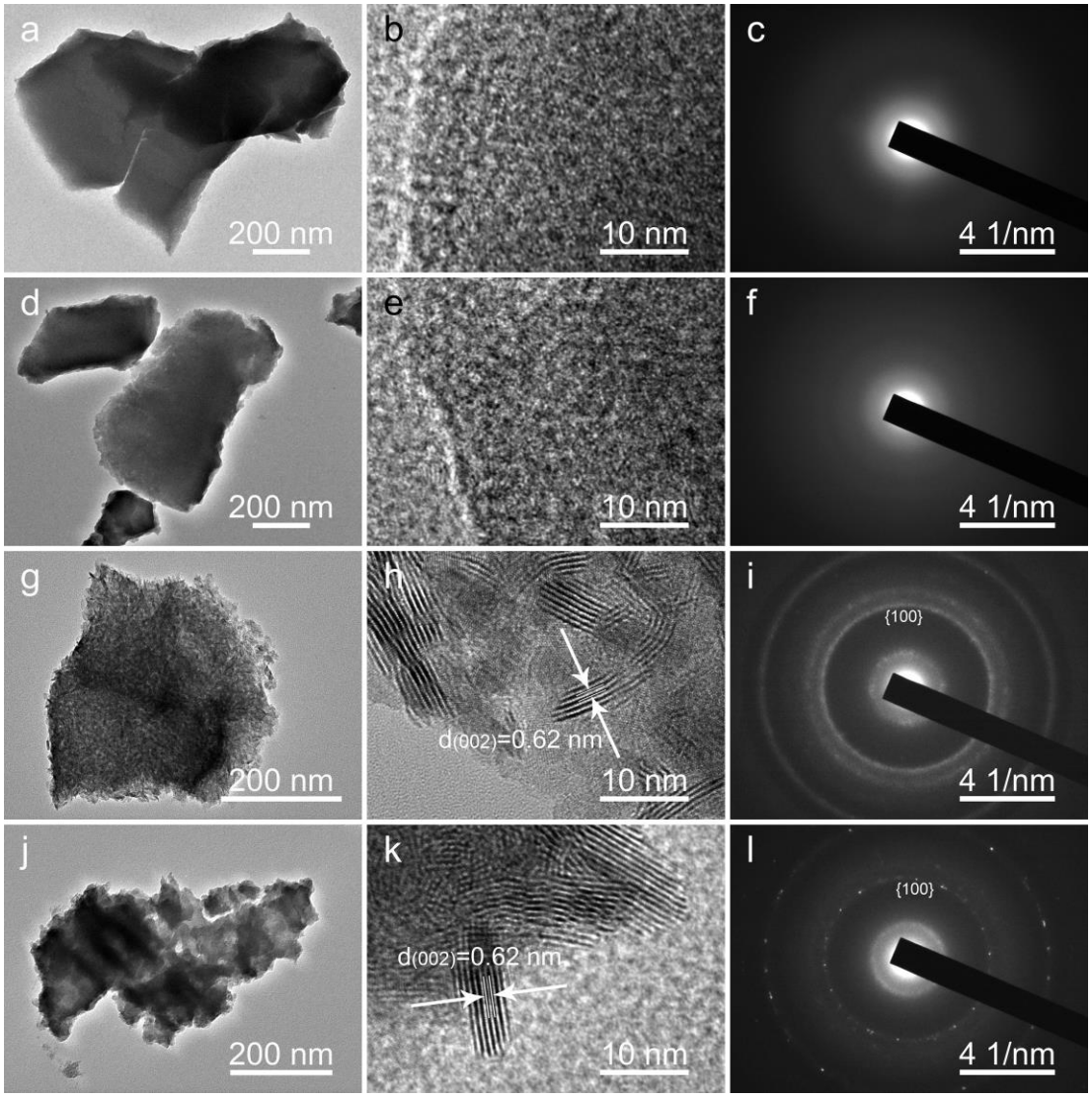

Fig. S4. Low magnification TEM images, high-resolution TEM images, and SAED patterns of nanoparticles deposited from the diluted catalyst suspension. (a, b, c) Tungsten sulfide annealed at 210 ºC. (d, e, f) Cobalt tungsten sulfide annealed at 210 ºC. (g, h, i) Tungsten sulfide annealed at 400 ºC. (j, k, l) Nickel tungsten sulfide annealed at 400 ºC. HR-TEM images (b, e) and SAED patterns (c, f) revealing the amorphous structure of tungsten sulfide and cobalt tungsten sulfide annealed at 210 ºC. Typical polycrystalline structures revealed by the HR-TEM images (h, k) and SAED patterns acquired from the tungsten sulfide and nickel tungsten sulfide annealed at 400 ºC. No crystalline nickel sulfide side-phase like Ni_3S_2 is observed from nickel tungsten sulfide annealed at 400 ºC from Fig. S4k, l, indicating that the catalyst is a single NiWS phase.

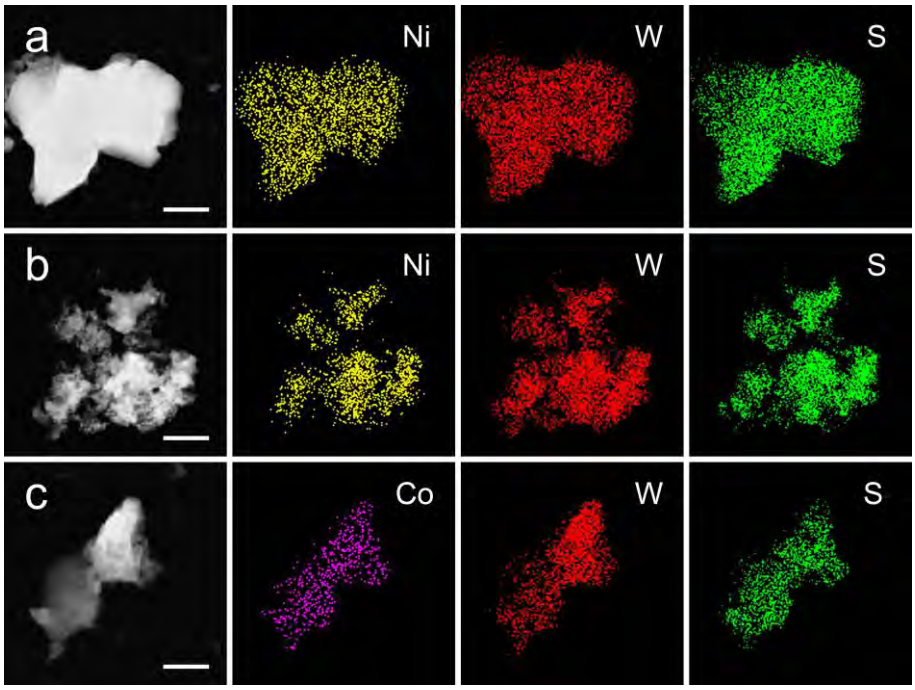

Fig. S5. Ni, W, and S elemental mapping images of three films deposited from the diluted catalyst suspension utilizing TEM: (a) NiWS film annealed at 180 ºC (scale bar = 500 nm), (b) NiWS film annealed at 400 ºC (scale bar = 500 nm), (c) CoWS annealed at 210 ºC (scale bar = 250 nm). The elemental mapping images indicate that Ni/Co, W, and S in the catalysts are homogeneously distributed.

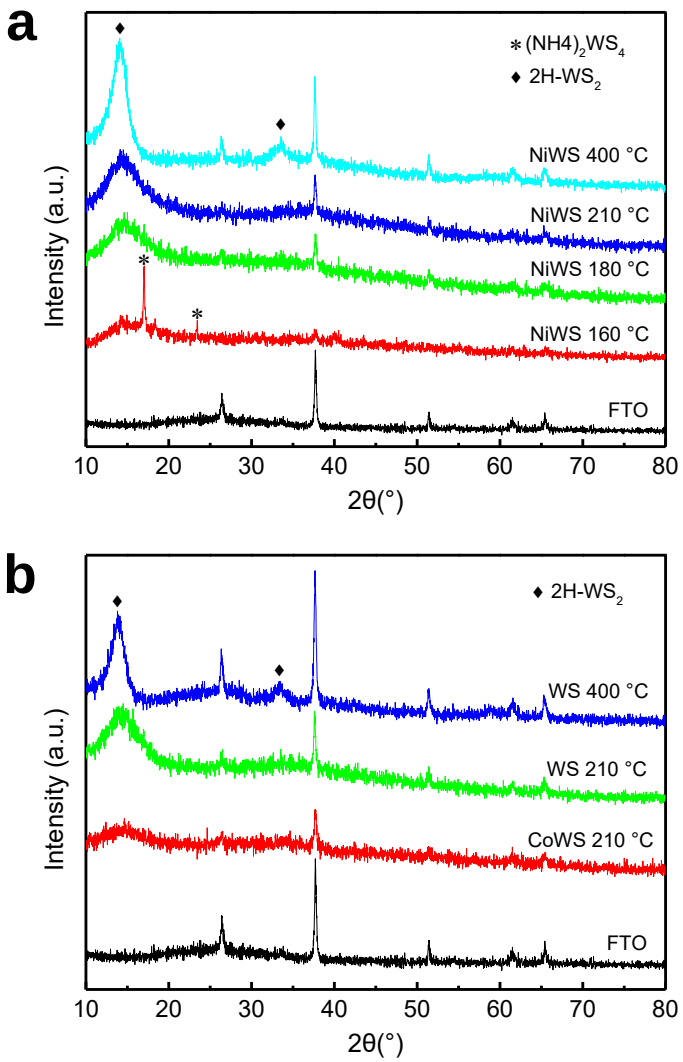

Fig. S6. XRD patterns acquired from the unpromoted, nickel and cobalt promoted tungsten sulfide films (WS, NiWS, CoWS) processed at 210 and 400 ºC on FTO-coated glass. (∗) represents the peaks from $(NH_4)_2WS_4$ which appear at 2θ of about. 17º and 23º corresponding to the [(120), (111)] and [(100), (101)] reflections (JCPDS card No. 48-1663). (♦) indicates the peaks from 2H-WS_2. The broad diffuse features at 2θ ca. 14º and 33º stem from the (002) and [(100), (101)] reflections of 2H-WS_2 (JCPDS card No. 08-0237), respectively.[S1] Nickel/Cobalt clusters or phase segregation of the NiWS into Ni_3S_2 and WS_2 is not observed as a result of the relatively small Ni or Co concentration and low processing temperature.[S2,S3]

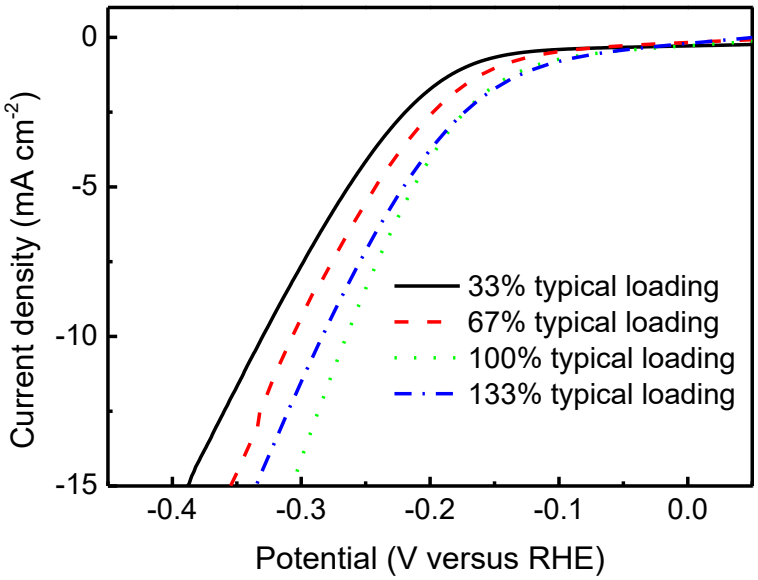

Fig. S7. Polarization curves of amorphous nickel tungsten sulfide films annealed at 210 ºC for different precursor mass loadings in 0.5 M H_2SO_4 at a scanning rate of 2 mV s^{-1}.

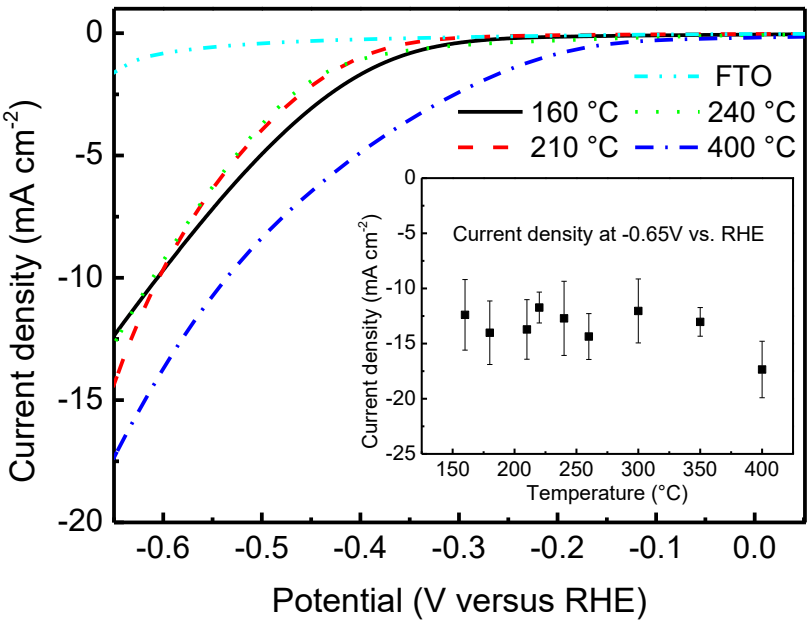

Fig. S8. Polarization curves of the unpromoted tungsten sulfide on FTO electrode for different annealing temperature. The potential scanning rate is 2 mV s^{-1}. The inset shows the corresponding current density at –0.65 V vs. RHE as a function of heating temperature, indicating poor catalytic activity of the unpromoted tungsten sulfide annealed below 400 °C. The error bars are presented according to several measurements on multiple samples.

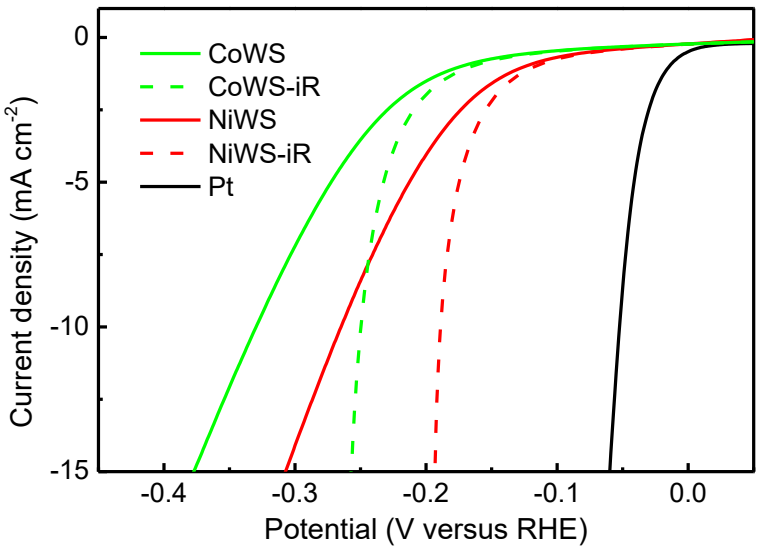

Fig. S9. Polarization curves of unpromoted, nickel and cobalt promoted amorphous tungsten sulfide films (WS, NiWS, and CoWS) on FTO electrode in 0.5 M H_2SO_4 at 2 mV s^{-1} with and without correction for iR losses (Fig. S11). The curve of the CoWS film is from the second polarization scan which shows a reduction process in the first scan. The curve of the Pt foil is shown for comparison.

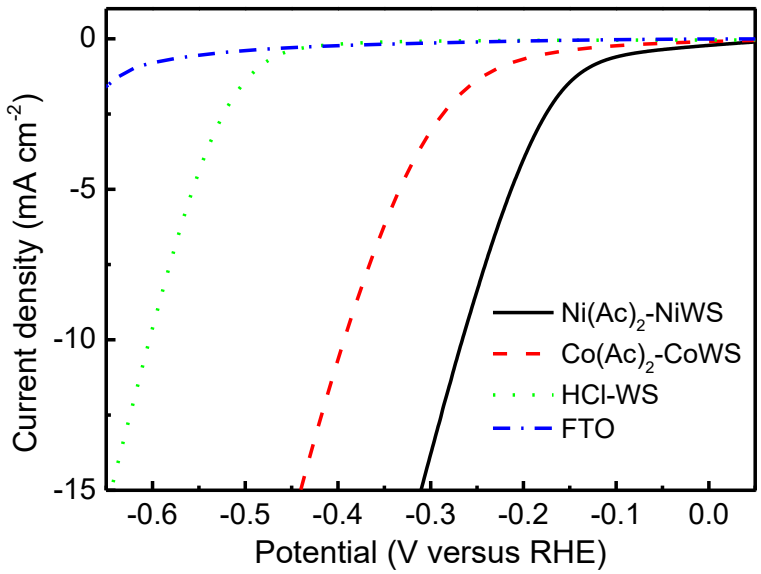

Fig. S10. Polarization curves of the catalyst films produced from different precursors. They are put together to estimate the effects of hydrogen and chloride ions. The curve acquired from pure FTO electrode is shown for comparison. Compared to previous results, similar catalytic activity is observed with nickel(II) acetate ($Ni(Ac)_2$) as the Ni^{2+} source, cobalt(II) acetate ($Co(Ac)_2$) as the Co^{2+} source, and HCl added to $(NH_4)_2WS_4$ as the precursor of the unpromoted tungsten sulfide. The results indicate that hydrogen ions do not make a big difference and the activity does not depend on the original Ni^{2+} or Co^{2+} counter ions.

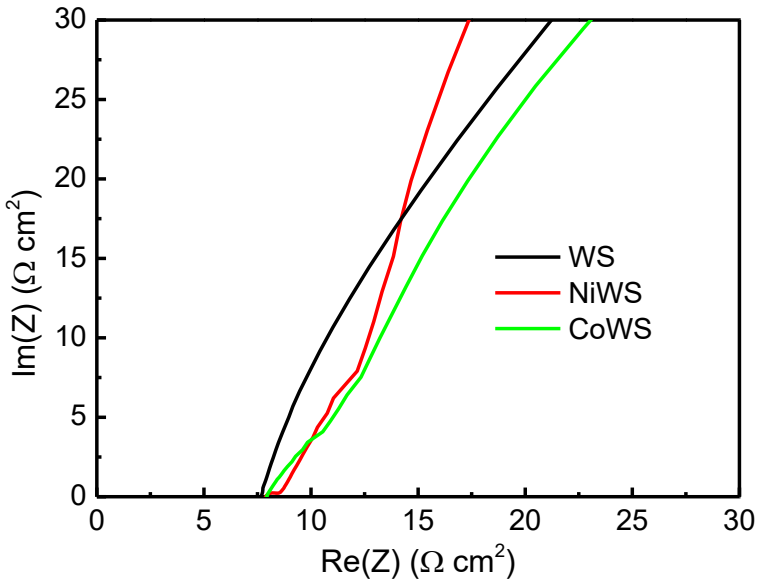

Fig. S11. Nyquist plots of the amorphous tungsten sulfide (WS), amorphous nickel tungsten sulfide (NiWS), and amorphous cobalt tungsten sulfide (CoWS) films on the FTO electrode at –0.10 V vs. RHE in 0.5 M H_2SO_4. All of the series resistances are in the range of 6-10 $\Omega\,cm^2$ and the average values are 7.7 $\Omega\,cm^2$ for WS_x, 7.9 $\Omega\,cm^2$ for amorphous NiWS, and 8.0 $\Omega\,cm^2$ for amorphous CoWS. The series resistance mainly comes from the catalyst film, FTO substrate, and electrolyte.

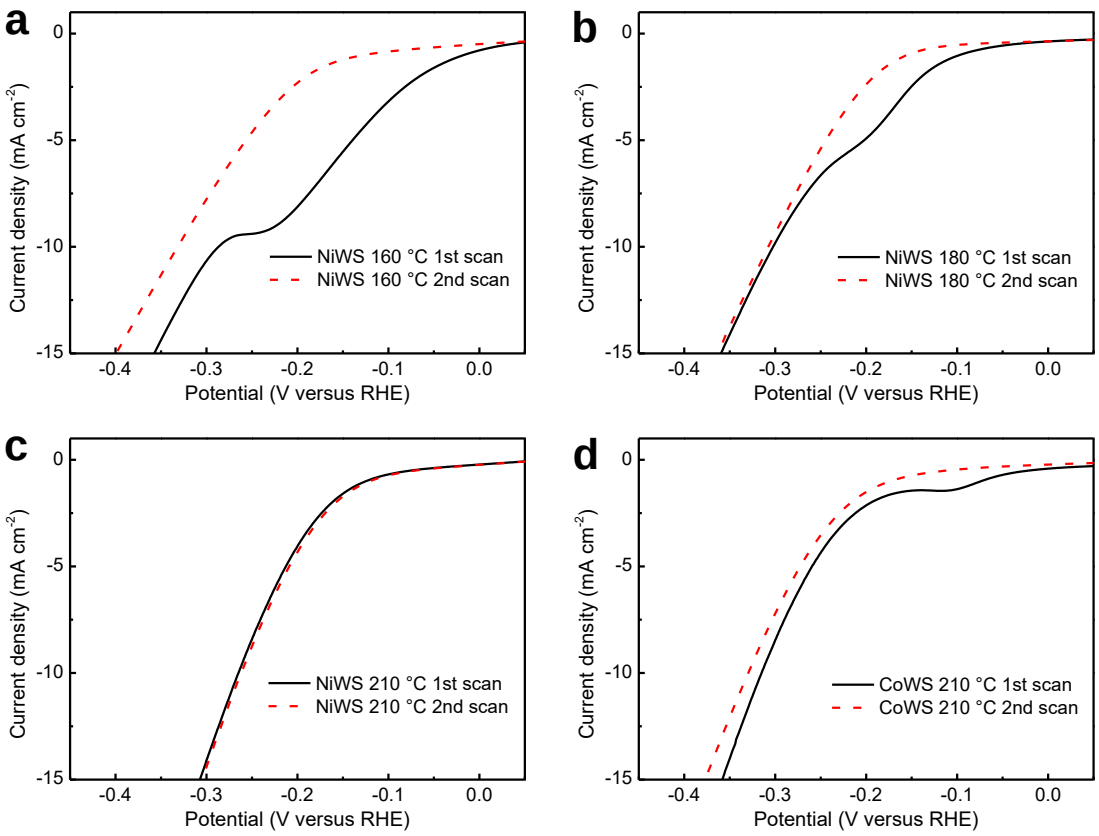

Fig. S12. First (dark line) and second (red dashed line) polarization curves of the freshly prepared catalyst films on FTO electrode in 0.5 M H_2SO_4 solution at a scanning rate of 2 mV s^{-1}. Nickel tungsten sulfide film annealed at 160 (a), 180 (b), 210 ºC (c), and cobalt tungsten sulfide film annealed at 210 ºC (d). The polarization curves in (a), (b) and (d) suggest a reduction process prior to hydrogen evolution as indicated in Fig. S12. This reduction peak is probably related to the interaction between Ni^{2+}/Co^{2+} and WS_4^{2-} as a result of incomplete thermolysis (Fig. S6).[S4,S5]

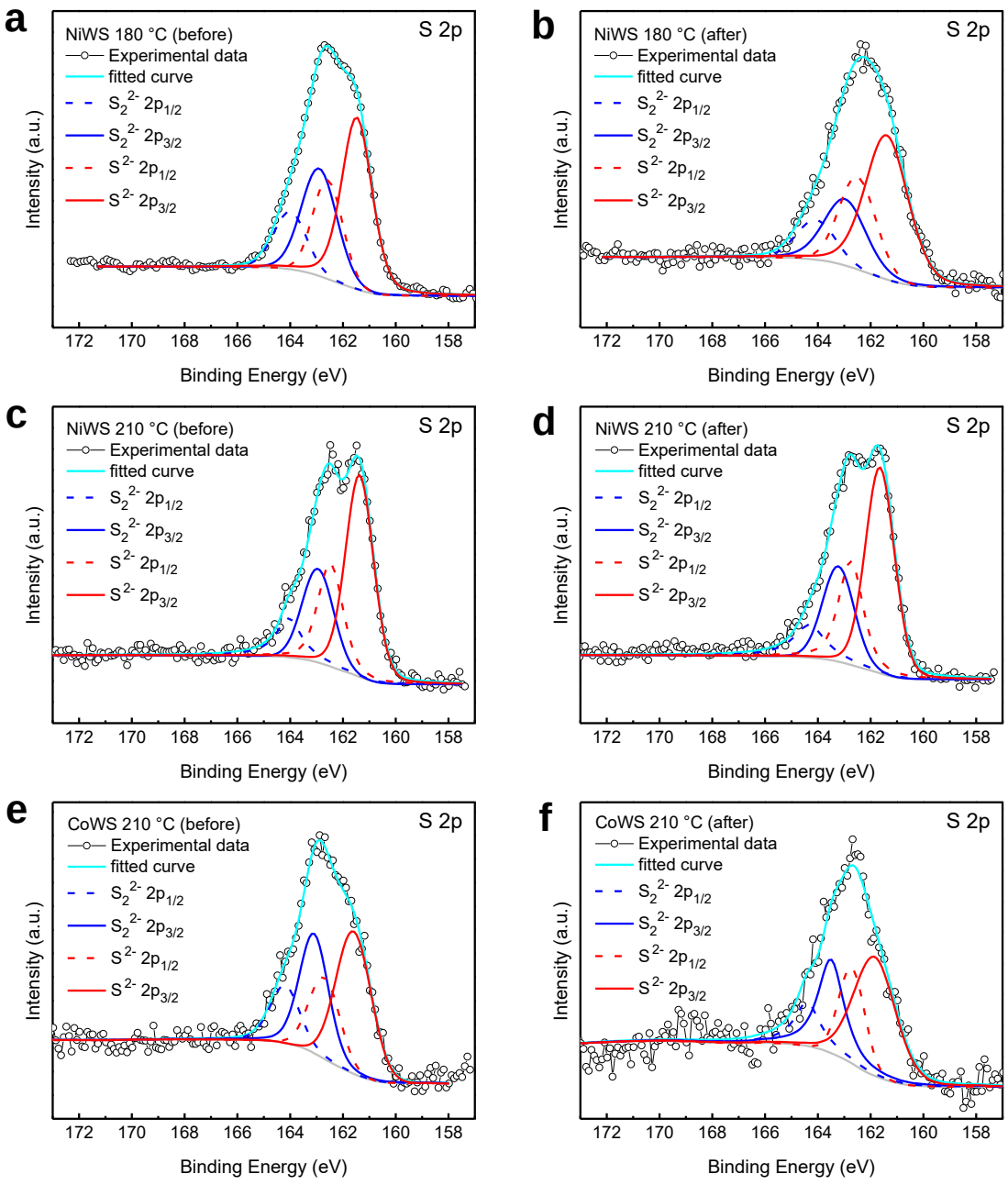

Fig. S13. S *2p* XPS spectra of the Ni and Co tungsten sulfide films before (a, c, e) and after (b, d, f) the first polarization experiment. Nickel tungsten sulfide is annealed at 180 (a, b) and 210 ºC (c, d). Cobalt tungsten sulfide is annealed at 210 ºC (e, f). The S 2p data are extracted from Fig. 5 in the manuscript and Figs. S19-S24 in Supporting Information. Similar reduction peak is also observed from amorphous molybdenum sulfide by electro-deposition[S6] or acidification.[S7] After the polarization testing, the S 2p spectrum of the NiWS annealed at 210 ºC changes slightly. For the NiWS

annealed at 180 ºC and CoWS annealed at 210 ºC, the S_2^{2-} features become weak, but do not disappear, indicating the reduction of portion S_2^{2-} to S^{2-}.

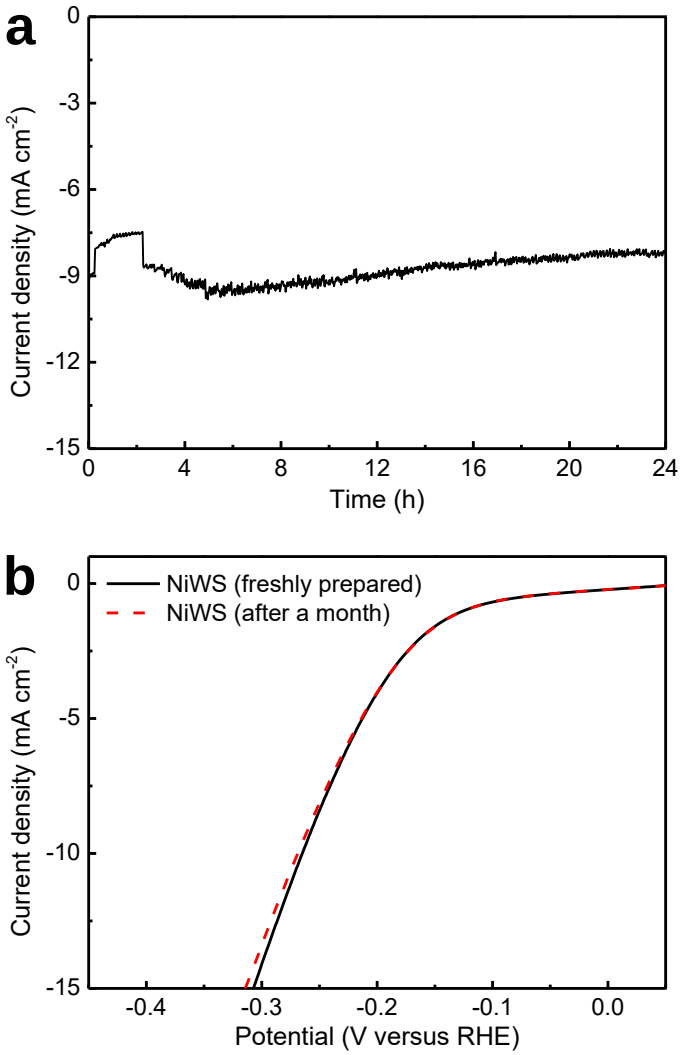

Fig. S14. (a) Long-term electrochemical stability test showing the variation of the current density measured from the amorphous nickel tungsten sulfide film on the FTO electrode at −0.25 V vs. RHE in 0.5 M H_2SO_4 with time. The current density is around 8.6 mA cm^{-2} and is sustained for 24 h, revealing the excellent catalytic activity and robustness of the materials. (b) Electrochemical activities of the freshly prepared amorphous nickel tungsten sulfide film (black line) on the FTO electrode in 0.5 M H_2SO_4 and the same catalyst left in air for a month (red dashed line).

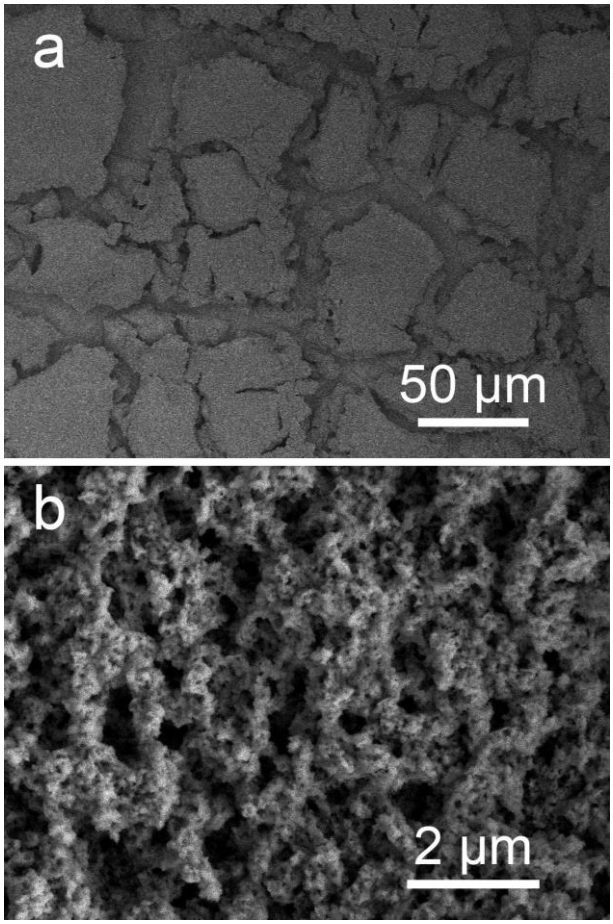

Fig. S15. (a, b) FE-SEM images of the amorphous nickel tungsten sulfide film after conducting the electrochemical stability test for 24 h.

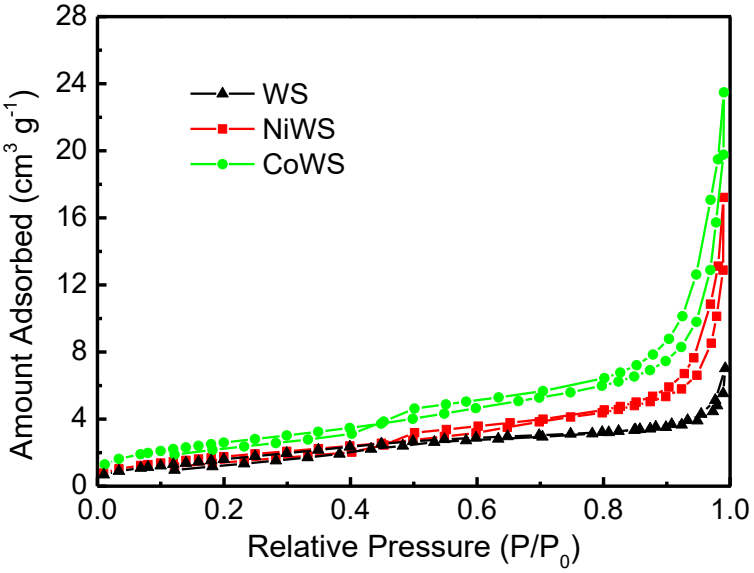

Fig. S16. Nitrogen adsorption-desorption isotherms of the amorphous tungsten sulfide (WS), amorphous nickel tungsten sulfide (NiWS), and amorphous cobalt tungsten sulfide (CoWS). The Brunauer-Emmett-Teller (BET) model is adopted to assess the surface area. The BET surface areas of the amorphous WS_x, NiWS, and CoWS are 6.31, 6.79, and 9.78 $m^2 g^{-1}$, respectively.

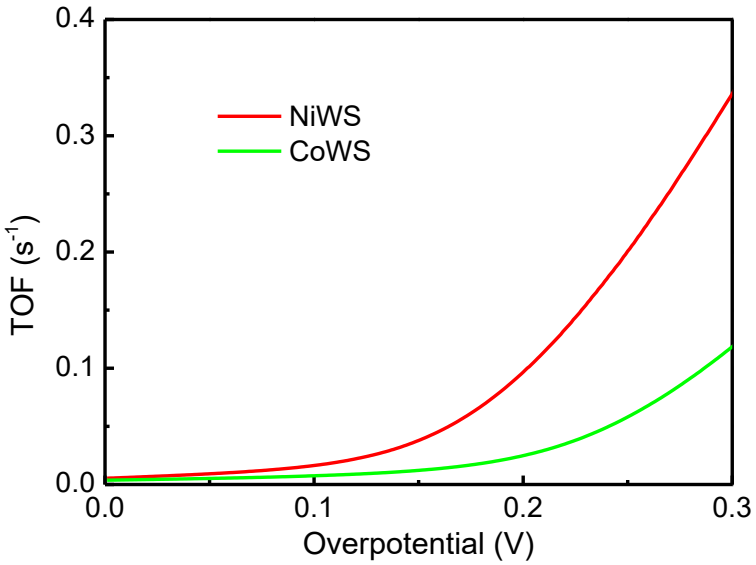

Fig. S17. Calculated lower limit turnover frequency versus overpotential of the amorphous nickel tungsten sulfide (NiWS, red line) and amorphous cobalt tungsten sulfide (CoWS, green line). The obtained results are based on data of the linear polarization curves from the catalyst films on FTO electrodes. The onset potential of amorphous WS_x is ~300 mV according to previous experimental results.

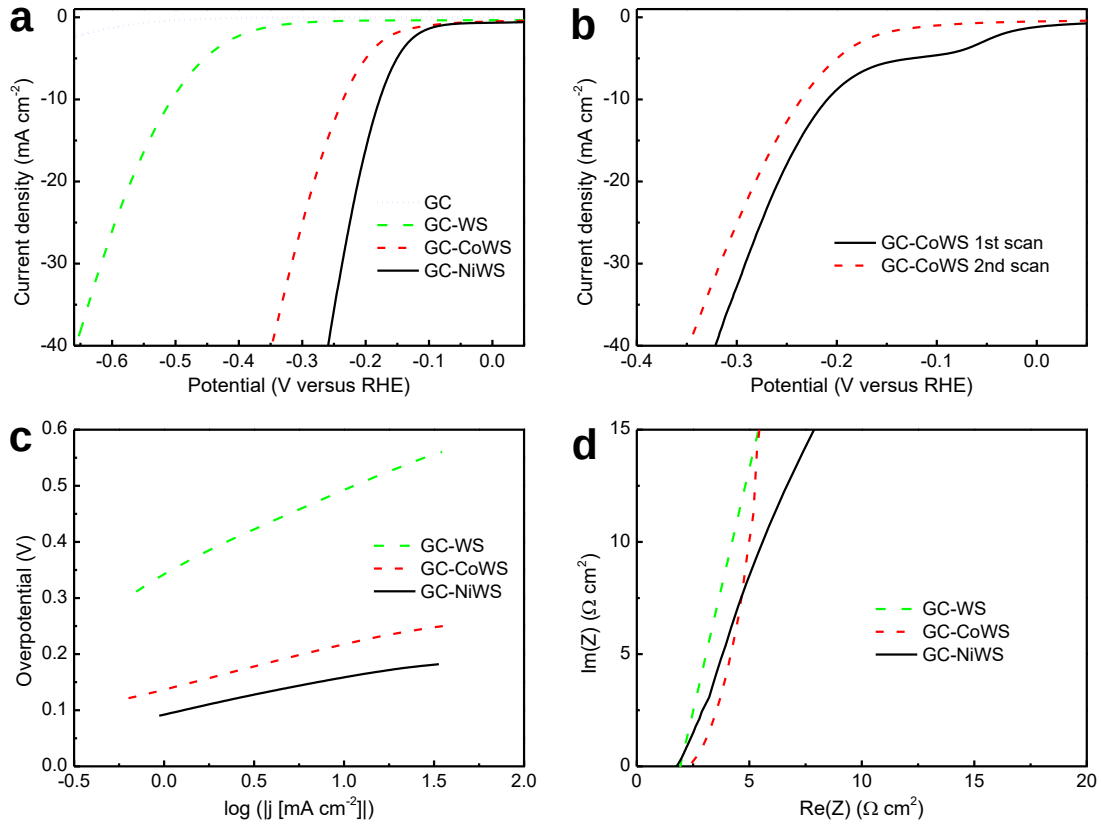

Fig. S18. HER activities of amorphous WS_x, CoWS, and NiWS films on GC electrodes. (a) Polarization curves of the catalyst films in 0.5 M H_2SO_4 at a scanning rate of 2 mV s^{-1}. The curve from CoWS in (a) is the second polarization scan. It also exhibits a reduction process in the first scan, as shown in (b). The HER performance of amorphous nickel tungsten sulfide on glassy carbon is quite impressive, as overpotentials of 260, 349, 658 mV are required to achieve a current density of 40 mA cm^{-2} for the amorphous WS_x, CoWS, and NiWS films, respectively. (c) Corresponding Tafel plots of the catalyst films after correction for iR losses. (d) Nyquist plots of the catalyst films at −0.10 V vs. RHE. Based on the Tafel plots in (c), the Tafel slopes and exchange current densities are obtained to be 142 mV dec^{-1} and 3.6 μA cm^{-2} for amorphous WS_x, 74 mV dec^{-1} and 13.4 μA cm^{-2} for amorphous CoWS, 56 mV dec^{-1} and 17.4 μA cm^{-2} for amorphous NiWS.

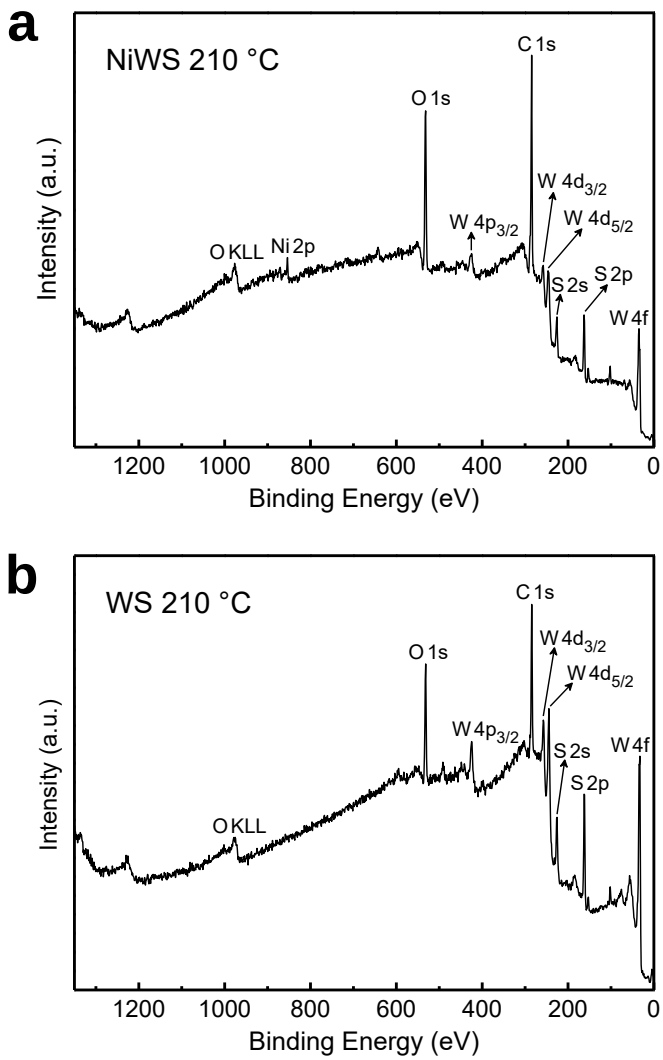

Fig. S19. (a) XPS survey spectrum of amorphous nickel tungsten sulfide (NiWS) annealed at 210 ^{o}C. The ratio of Ni: W: S is 0.36:1:2.78. (b) XPS survey spectrum of the amorphous tungsten sulfide (WS) annealed at 210 ^{o}C. The S to W ratio is 2.62:1.

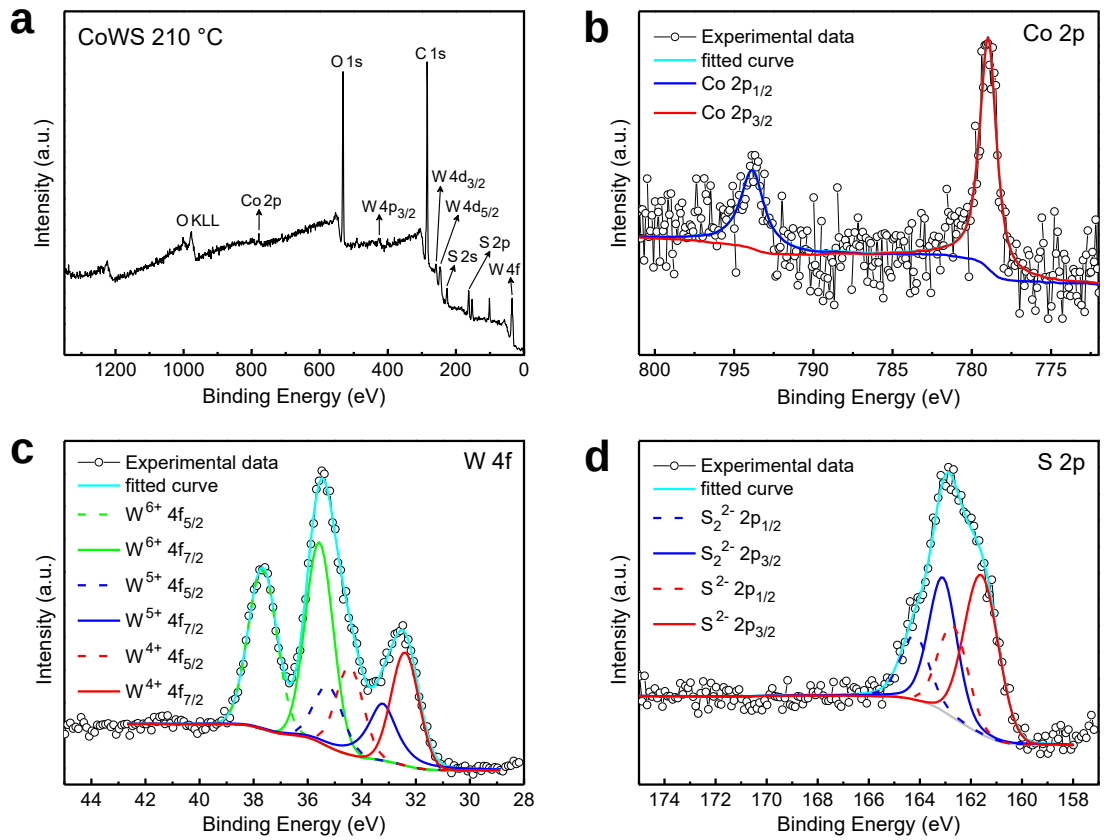

Fig. S20. XPS spectra of the amorphous cobalt tungsten sulfide (CoWS) annealed at 210 ºC: (a) XPS survey spectrum, (b) Co 2p region, (c) W 4f region, and (d) S 2p region. The Co:W:S ratio is 0.36:1:2.86. In the Co 2p spectrum in (b), the two peaks correspond to Co $2p_{1/2}$ and $2p_{3/2}$ binding energies. Similar to the NiWS annealed at 210 ºC, the bonding states of the amorphous CoWS are quite different from those of WS_x in the W 4f and S 2p regions. The present W^{6+} and S^{2-} features are more obvious than those of WS_x. Moreover, the relative intensity ratio of S_2^{2-} to S^{2-} is even larger than that from the NiWS annealed at 210 ºC.

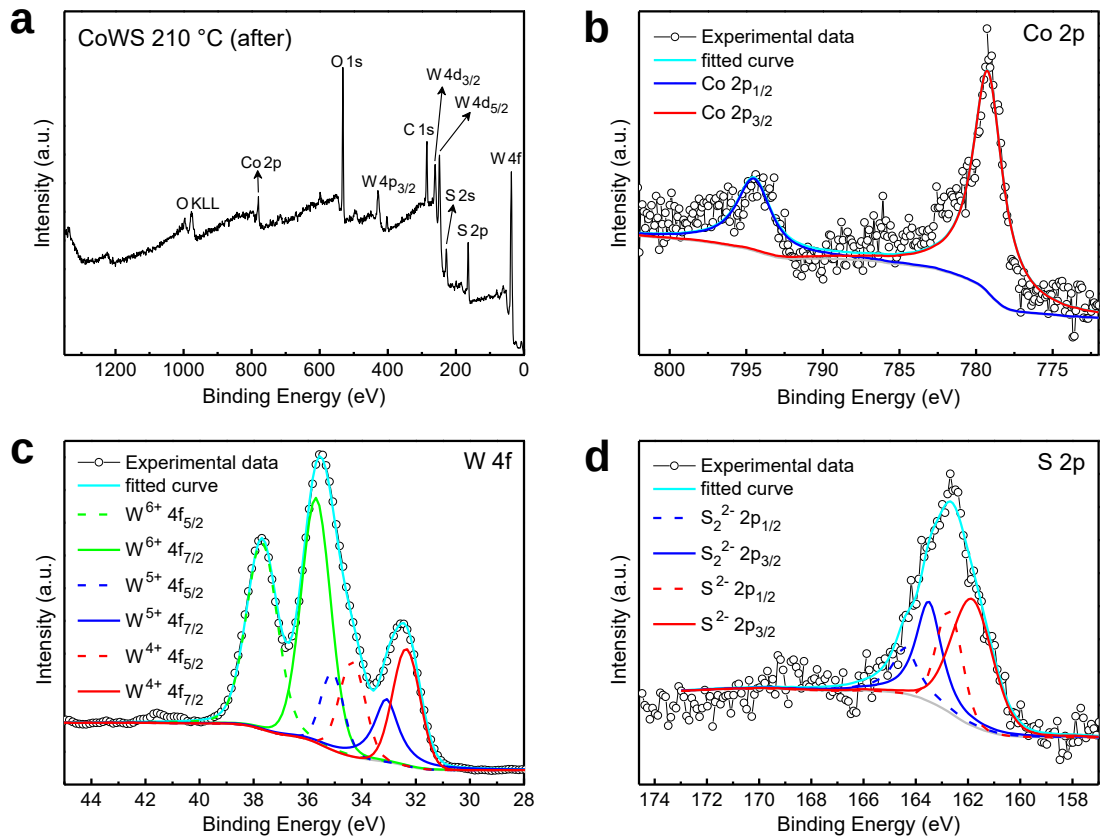

Fig. S21. XPS spectra of the amorphous cobalt tungsten sulfide (CoWS) annealed at 210 ºC after the first polarization experiment: (a) XPS survey spectrum, (b) Co 2p region, (c) W 4f region, and (d) S 2p region. After testing, the Co 2p and W 4f spectra display relatively small changes. However, the S^{2-} signal increases and S_2^{2-} signal decreases obviously. The S 2p XPS spectra indicate that portion S_2^{2-} is reduced to S^{2-} after the voltammetry measurement, comporting with the reduction peak in the polarization curve in Fig. S11(d).

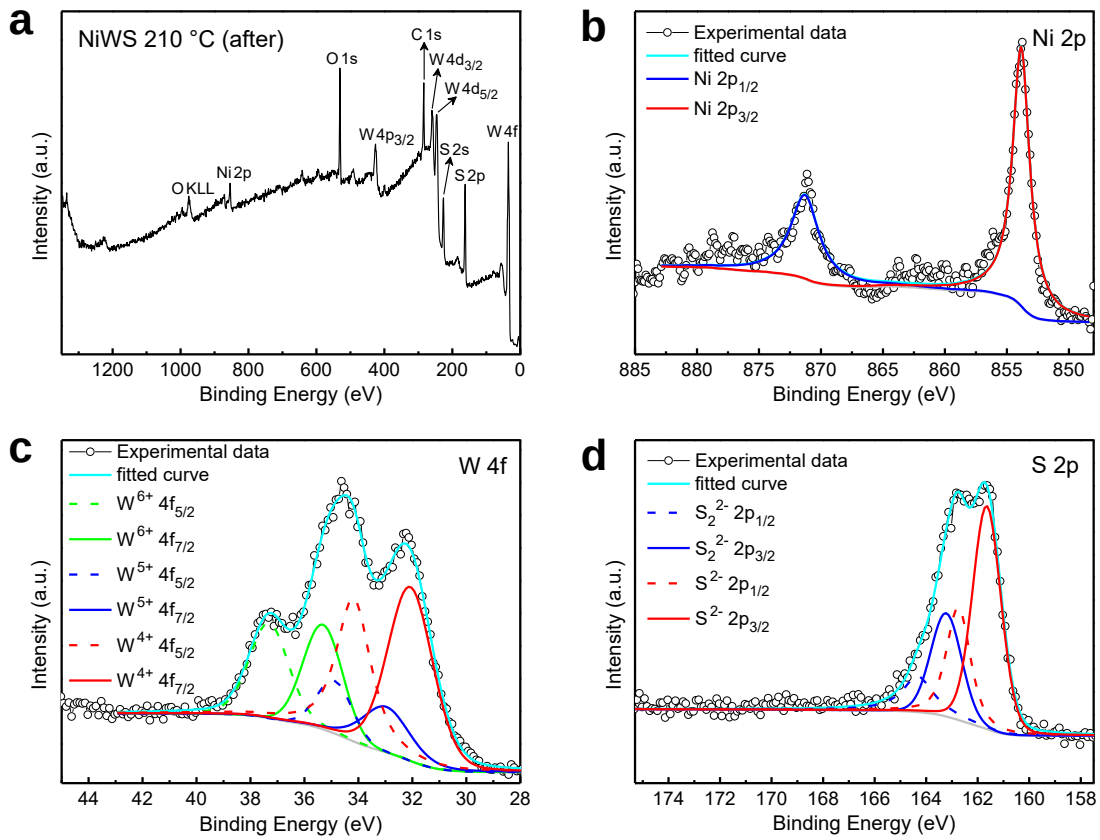

Fig. S22. XPS spectra of the amorphous nickel tungsten sulfide (NiWS) annealed at 210 ºC after the first polarization experiment: (a) XPS survey spectrum, (b) Ni 2p region, (c) W 4f region, and (d) S 2p region. In contrast to the XPS spectra of the amorphous NiWS annealed at 180 ºC and CoWS at 210 ºC, the XPS spectra in the Ni 2p, W 4f, and S 2p regions of the amorphous NiWS annealed at 210 ºC present little changes after the polarization scan. This result reveals the stability of the Ni-promoted catalyst annealed at 210 ºC. This is in accordance with the linear sweep voltammetry shown in Fig. S11(c).

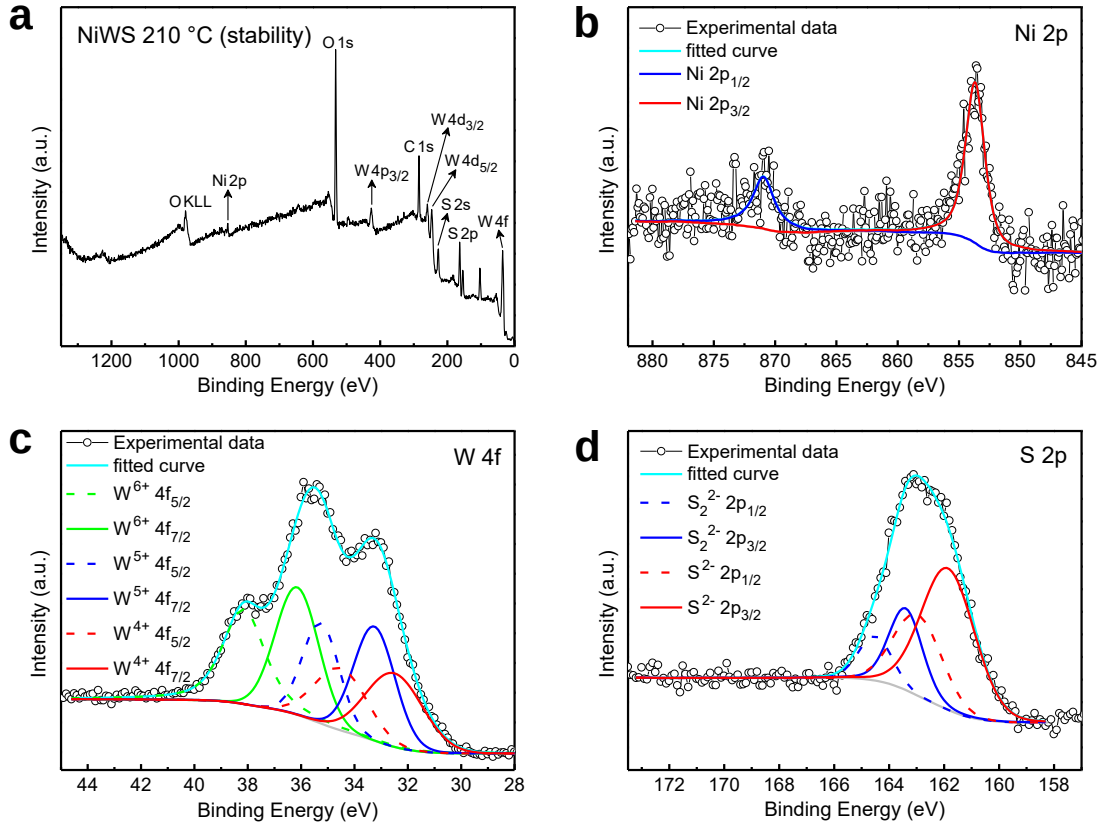

Fig. S23. XPS spectra of the amorphous nickel tungsten sulfide (NiWS) annealed at 210 °C after conducting the electrocatalytic reaction for 3 h: (a) XPS survey spectrum, (b) Ni 2p region, (c) W 4f region, and (d) S 2p region. After the HER test, the peak positions of Ni $2p_{1/2}$ and $2p_{3/2}$ in (b) alter a little. The W^{6+} signal in the W 4f region and S_2^{2-} signal in S 2p region slightly increases and decreases, respectively. In addition, the W^{5+}/W^{4+} ratio becomes larger after the HER testing.

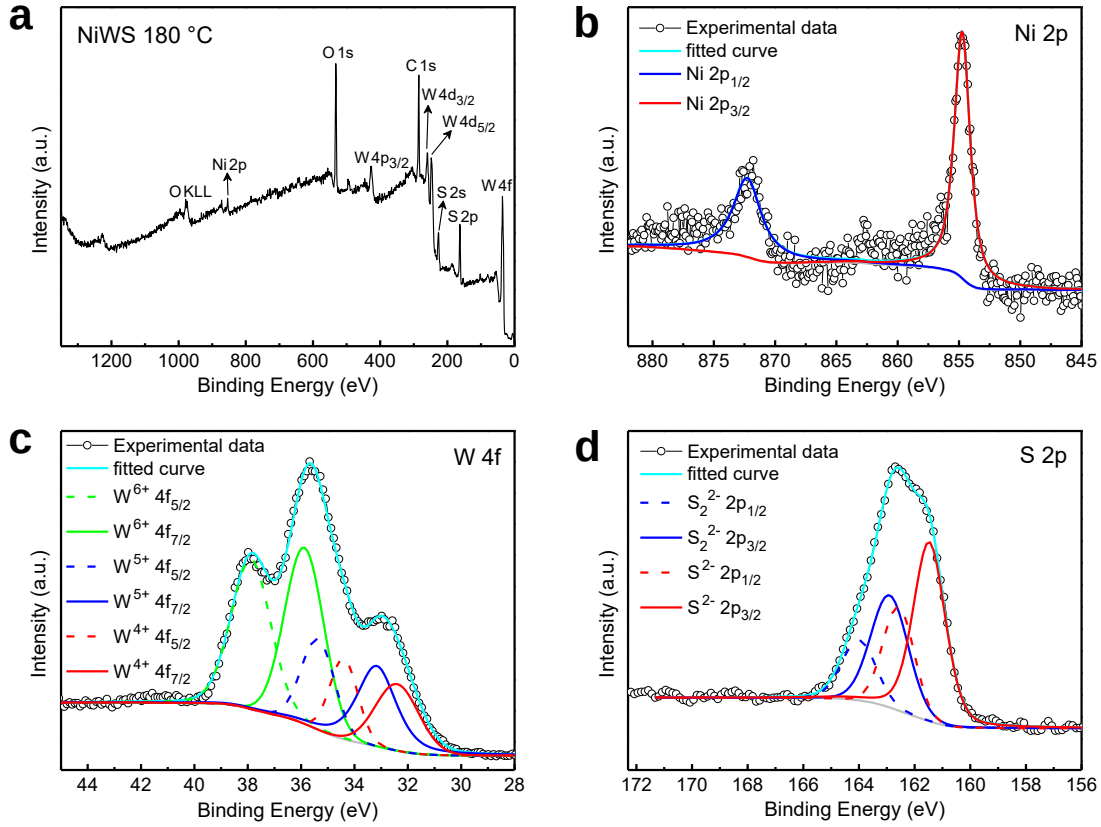

Fig. S24. XPS spectra of the amorphous nickel tungsten sulfide (NiWS) annealed at 180 ºC: (a) XPS survey spectrum, (b) Ni 2p region, (c) W 4f region, and (d) S 2p region. As shown in (b), the two peaks correspond to the Ni $2p_{1/2}$ and $2p_{3/2}$ binding energies and their positions are close to those of the NiWS annealed at 210 ºC. However, the W 4f spectra are different in the two samples. The W^{5+} and W^{6+} signals are more obvious and the W^{4+} signal is relatively small in the NiWS annealed at 180 ºC. In the S 2p region, the S_2^{2-} peaks are stronger than that in the NiWS annealed at 210 ºC but they decrease after the polarization scan, as shown in Fig. S24.

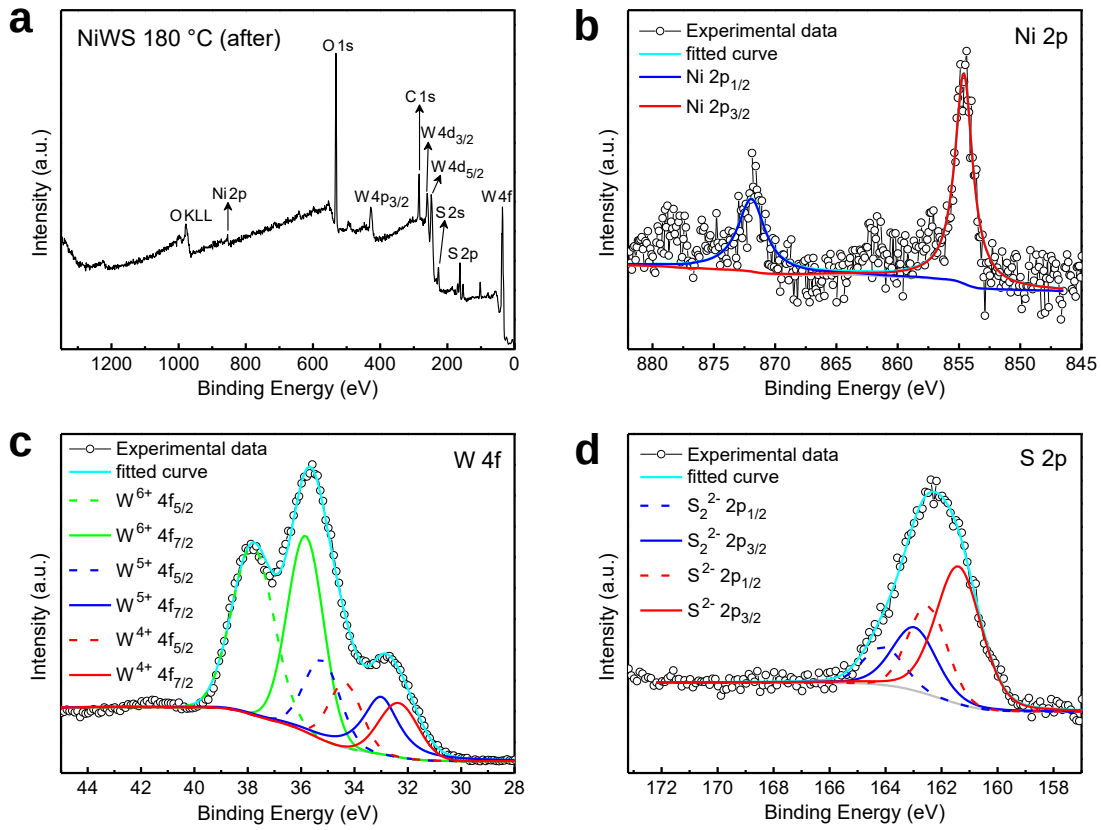

Fig. S25. XPS spectra of the amorphous nickel tungsten sulfide (NiWS) annealed at 180 ºC after the first polarization experiment: (a) XPS survey spectrum, (b) Ni 2p region, (c) W 4f region, and (d) S 2p region. After the polarization scan, relatively small changes are observed in the Ni 2p and W 4f spectra. However, the S_2^{2-} and S^{2-} signals decreases and increases, respectively. This indicates the reduction of portion S_2^{2-} to S^{2-}. The relative intensity of the S_2^{2-} peak after the test is even lower than that in the amorphous NiWS annealed at 210 ºC.

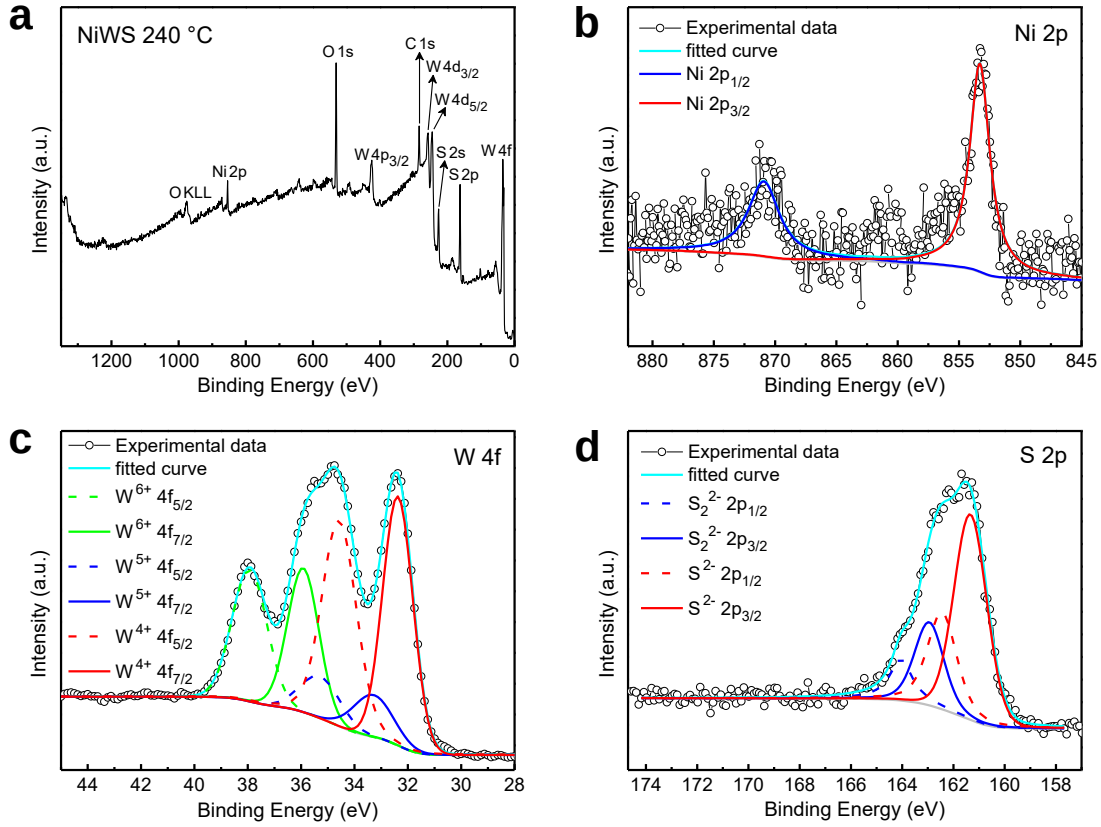

Fig. S26. XPS spectra of the amorphous nickel tungsten sulfide (NiWS) annealed at 240 ºC: (a) XPS survey spectrum, (b) Ni 2p region, (c) W 4f region, and (d) S 2p region. The two peaks in the Ni 2p spectrum which correspond to the Ni $2p_{1/2}$ and $2p_{3/2}$ binding energies indicate the incorporation of Ni element. Compared to the amorphous NiWS annealed at 210 ºC, the peak intensity ratios of W^{5+}/W^{4+} in the W 4f region and S_2^{2-}/S^{2-} in the S 2p region decrease. The W^{6+} peaks in the W 4f spectrum are still more apparent than those from the unpromoted catalyst.

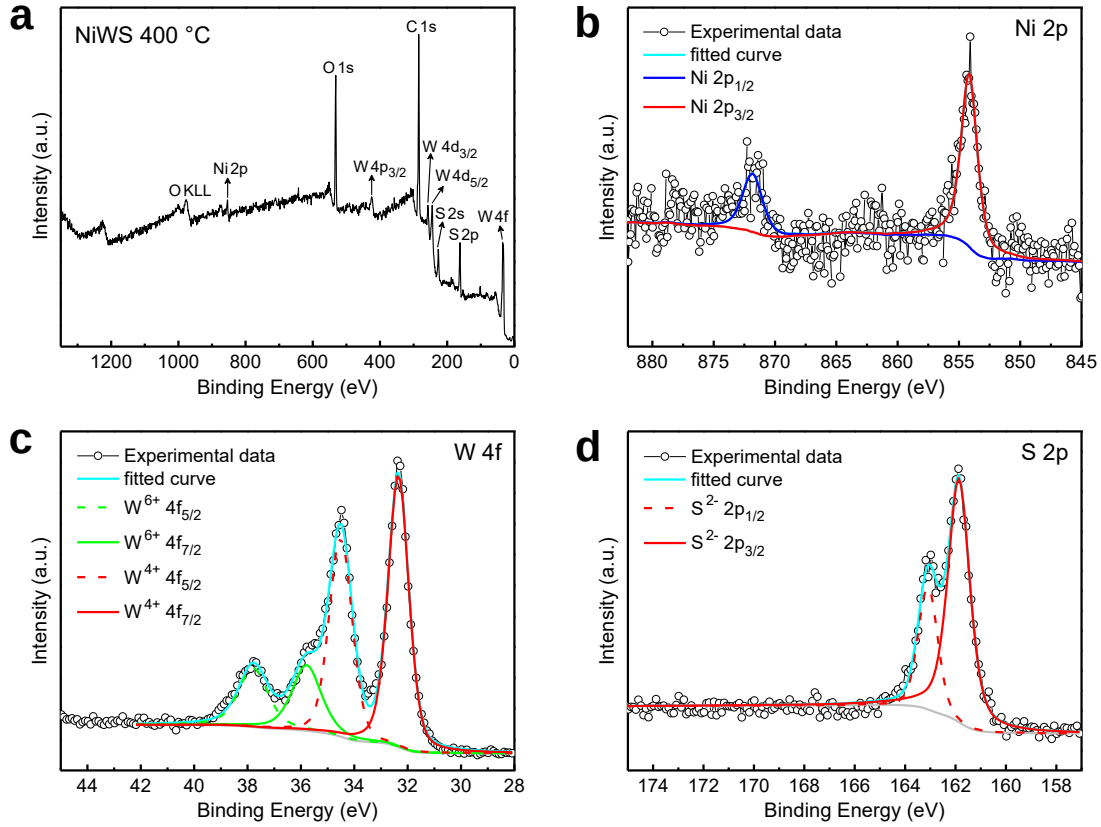

Fig. S27. XPS spectra of the nickel tungsten sulfide (NiWS) annealed at 400 ºC: (a) XPS survey spectrum, (b) Ni 2p region, (c) W 4f region, and (d) S 2p region. In the Ni 2p region, the two peaks correspond to the Ni $2p_{1/2}$ and $2p_{3/2}$ binding energies. The peak position of Ni $2p_{3/2}$ is a little larger than that from the NiWS annealed at 210 ºC. But in the W 4f and S 2p regions, the W^{5+} and S_2^{2-} signals vanish and the W^{4+} and S^{2-} peaks become the main features of the spectra. Besides, the W^{6+} peaks representing oxidation of W still exist. The XPS data coincide with the previous TGA, XRD, TEM, and SAED results.

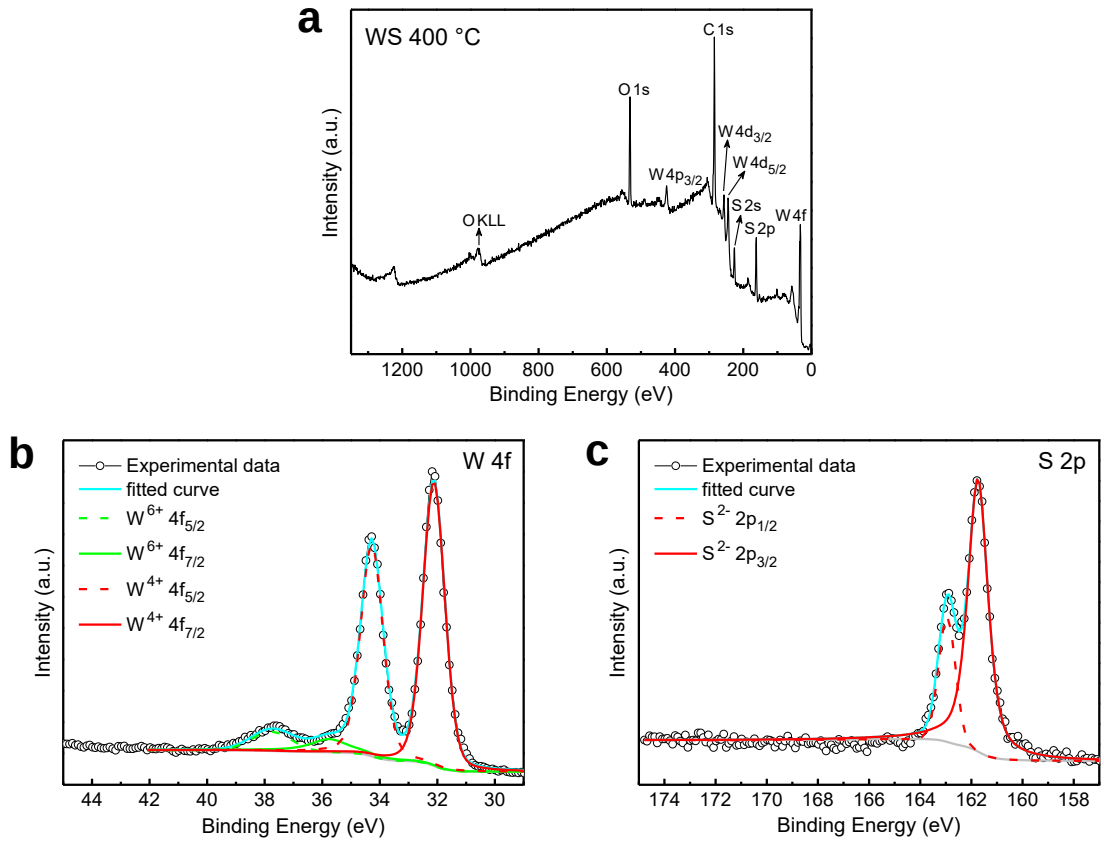

Fig. S28. XPS spectra of the unpromoted tungsten sulfide (WS) annealed at 400 ºC: (a) XPS survey spectrum, (b) W 4f region, and (c) S 2p region. Similar to the case from the NiWS annealed at 400 ºC, the W^{5+} and S_2^{2-} signals disappear and the W^{4+} and S^{2-} signals become the main features of the W 4f and S 2p spectra for the unpromoted tungsten sulfide annealed at 400 ºC. In addition, the W^{6+} peaks are smaller compared to those in the promoted catalyst. This is similar to the case from the NiWS annealed at 210 ºC. The XPS results further confirm that the tungsten sulfide annealed at 400 ºC is a crystalline 2H-WS_2.

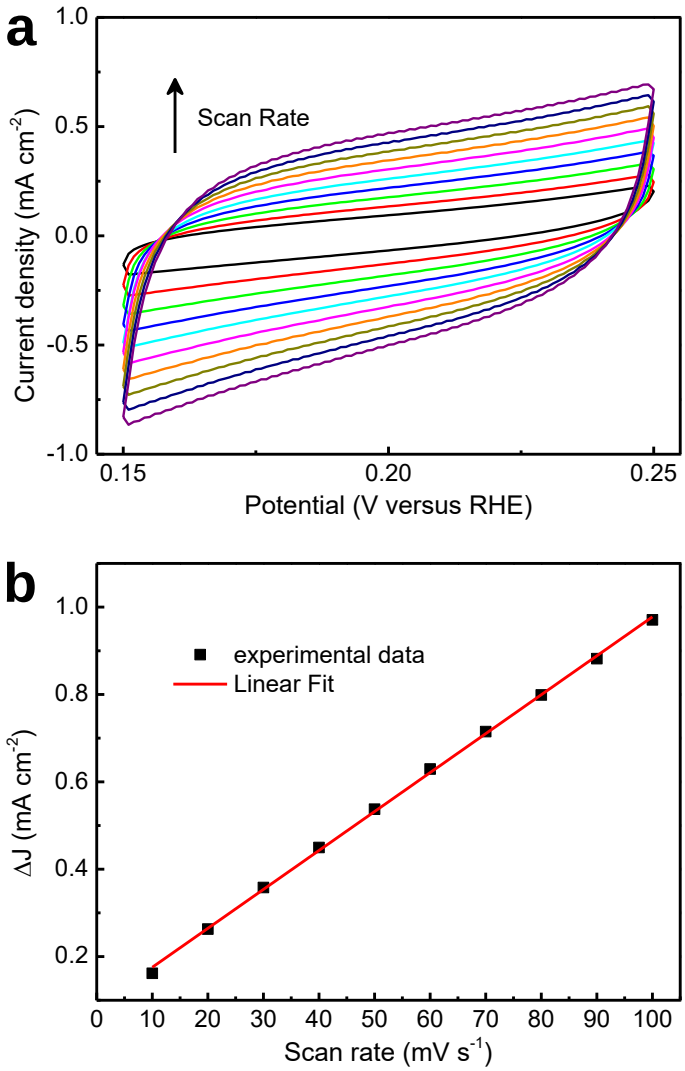

Fig. S29. (a) Cyclic voltammograms of the amorphous cobalt tungsten sulfide (CoWS) film annealed at 210 °C on FTO electrode acquired at different scanning rates (10-100 mV s^{-1}) in 0.5 M H_2SO_4. (b) Corresponding scanning rate dependence of the current density at 0.20 V vs. RHE. The calculated double layer capacitance of amorphous CoWS is 4460 μF cm^{-2}.

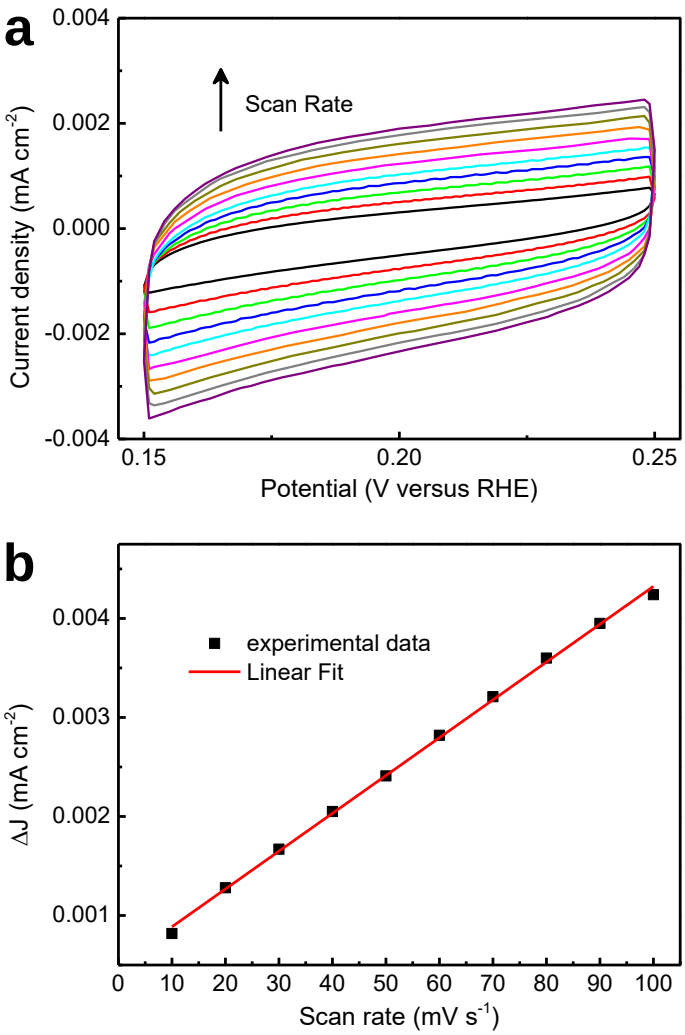

Fig. S30. (a) Cyclic voltammograms of the amorphous tungsten sulfide film annealed at 210 ºC obtained at different scanning rates (10-100 mV s^{-1}). (b) Corresponding scanning rate dependence of the current density at 0.20 V vs. RHE. The calculated capacitance of amorphous WS_x is 19 μF cm^{-2}. By normalizing the capacitance to the value of WS_x, the relative geometric surface areas (S^*_{echem}) are 1, 234, and 342 for amorphous WS_x, CoWS, and NiWS, respectively.

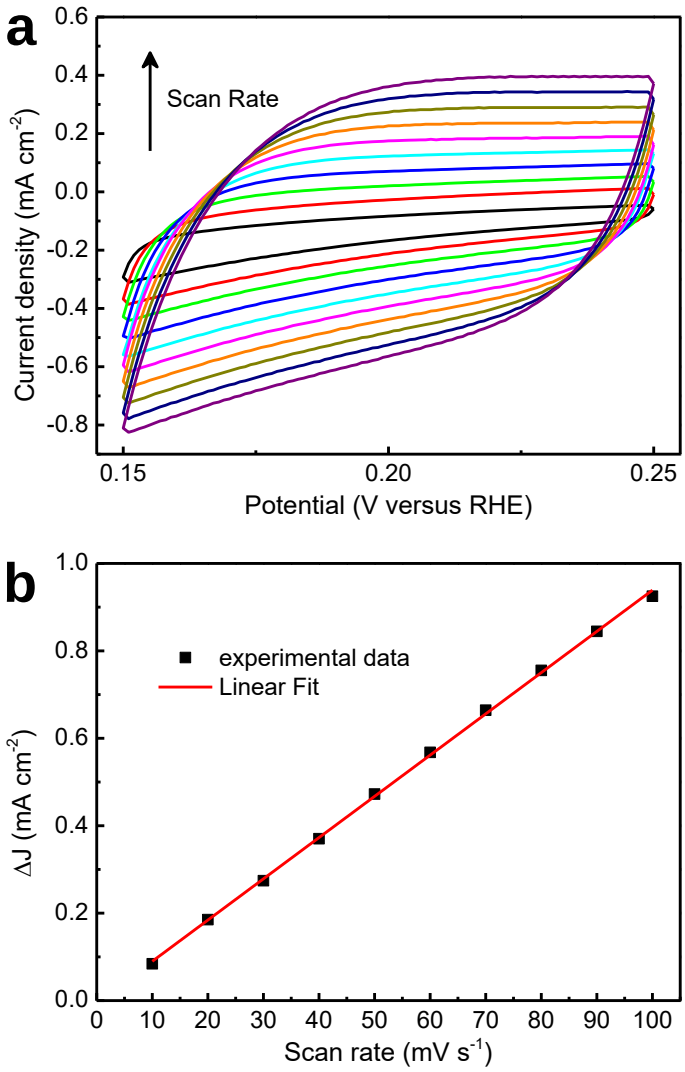

Fig. S31. (a) Cyclic voltammograms of the amorphous NiWS annealed at 180 °C obtained at different scanning rates (10-100 mV s^{-1}). (b) Corresponding scanning rate dependence of the current density at 0.20 V vs. RHE. C_{dl} of the amorphous NiWS annealed at 180 °C is 4715 μF cm^{-2} and S^{*}_{echem} is 248. These values are in accord with the previous HER performance, indicating that the activity of the amorphous NiWS annealed at 180 °C is inferior to the amorphous NiWS annealed at 210 °C, but it is still much better than that of the amorphous WS_x annealed at 210 °C.

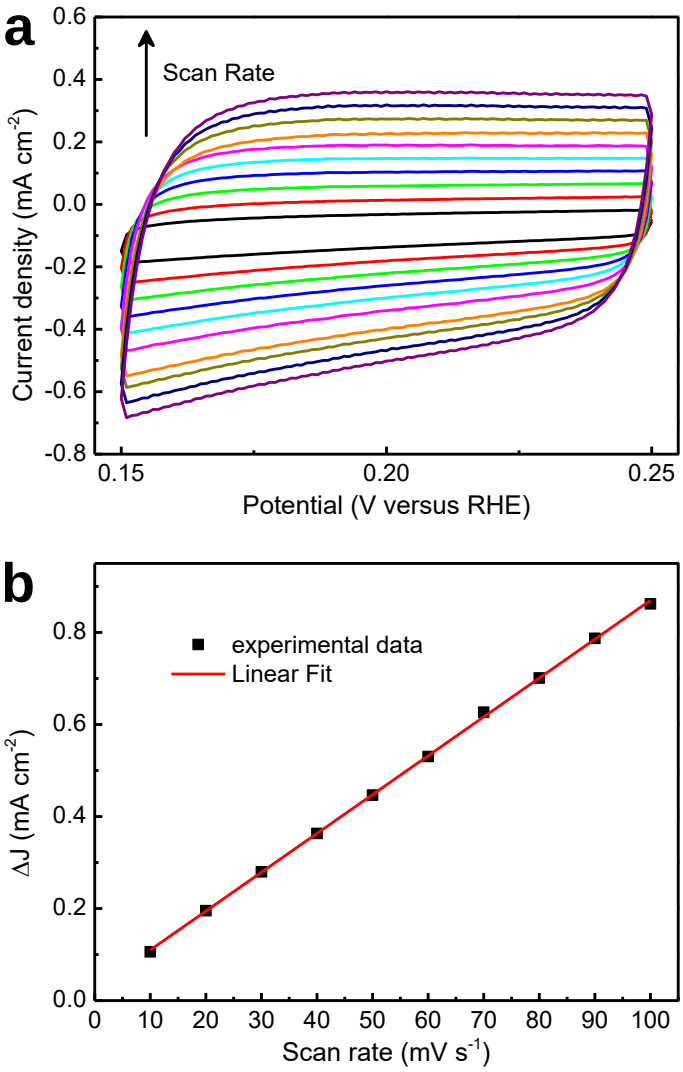

Fig. S32. (a) Cyclic voltammograms of the amorphous NiWS annealed at 240 °C obtained at different scanning rates (10-100 mV s^{-1}). (b) Corresponding scanning rate dependence of the current density at 0.20 V vs. RHE. C_{dl} of the amorphous NiWS annealed at 240 °C is 4220 μF cm^{-2} and S^{*}_{echem} is 222. Similar to the case in the NiWS annealed at 180 °C, these values are smaller than those from the NiWS annealed at 210 °C, but they are still much larger than those from the amorphous WS_x. This is in line with the previous HER activity.

Tafel analysis and HER mechanism

In an acidic medium, hydrogen evolution is considered to involve the following three elementary reactions:[S8]

$H_3O^+ + e^- + cat \Leftrightarrow H\text{-}cat + H_2O$, discharge step (Volmer reaction) (1)

$H\text{-}cat + H\text{-}cat \Leftrightarrow H_2 + 2cat$, recombination step (Tafel reaction) (2)

$H_3O^+ + e^- + H\text{-}cat \Leftrightarrow H_2 + cat + H_2O$, desorption step (Heyrovsky reaction) (3)

The Tafel slope is an intrinsic property of electrocatalysts and determined by the rate-limiting step of HER. In the Volmer-Tafel mechanism, if a fast discharge reaction is followed by a rate-determining recombination reaction, a Tafel slope of 29 mV dec^{-1} should be observed, as is well known for Pt(111). In the Volmer-Heyrovsky mechanism, if the discharge reaction is fast and the electrochemical desorption reaction is slow, the Tafel slope should be 38 mV dec^{-1}. In both mechanisms, a rate-determining discharge reaction results in a theoretical Tafel slope of 116 mV dec^{-1}.

The Tafel slope depends on many factors such as the reaction pathway and adsorption conditions in a complex way and the influencing factors in Tafel analysis are not completely clear with respect to MX_2-based catalysts.[S8] More work is needed to elucidate the HER mechanism clearly.

Calculation of the lower limit for turnover frequency (TOF).

The method used to determine the lower limit of the TOF values shown below is similar to that described in Refs. S9 and S10. The relative roughness factor is obtained from the BET and XPS measurements[S9] and the hypothetical geometry of the 2H-WS_2 surface is adopted to calculate the surface site density[S10] in order to derive the lower limit of the TOF values at the specified current density.

In the typical procedure, the initial loading of $(NH_4)_2WS_4$ is 6 mg cm^{-2} for unpromoted and promoted catalyst films. The elemental composition is calculated from XPS spectra and considering the fixed W content, the final loading values are 4.18 mg cm^{-2} for WS_x, 5.07 mg cm^{-2} for amorphous NiWS, and 5.11 mg cm^{-2} for amorphous CoWS. The relative roughness factor (RF_{BET}) is defined as the quotient of the actual surface area of the catalyst films divided by the FTO substrate area. Utilizing the BET data, the RF_{BET} values are 264.3 for WS_x, 344.3 for amorphous NiWS, and 499.5 for amorphous CoWS. By normalization of these values, the relative geometric surface areas (S^*_{geom}) are obtained to be 1, 1.30, and 1.89 for amorphous WS_x, NiWS and CoWS, respectively.

To estimate the upper limit for the surface density of active sites, it is assumed that all the surface sites are catalytically active. The quantity of surface sites is calculated based on the geometry of 2H-WS_2.[S10] As an approximation, it is postulated that the average area of surface sites has the same value as the WS_2 unit in the 2H-WS_2 basal planes.[S10] The calculated surface area of a WS_2 unit is 0.26 nm^2, according to the hexagonal arrangement of sulfur atoms and S-S bond length of 0.318 nm on the 2H-WS_2 surface.[S11]

The lower limit TOF per site at a given current density of j mA cm^{-2} is calculated as follows:

$$\text{TOF} = j\ mA\,cm^{-2} \times 1\,cm^2 \times \frac{1}{1.602 \times 10^{-19}\ C} \times \frac{1}{2} \times \frac{1}{RF_{BET} \times 1\,cm^2 / 0.26\,nm^2}$$

$$= 8.2 \times \frac{j}{RF_{BET}}\ s^{-1}$$

Using this formula, the TOF values of hydrogen molecules evolved per second are calculated to be 0.34 and 0.12 s^{-1} at 300 mV overpotential for the amorphous NiWS and CoWS films on FTO electrodes, respectively.

Table S1. Comparison of various MX_2-based HER catalysts in acid media.

Catalyst	b ($mV\ dec^{-1}$)	j_0 ($\mu A\ cm^{-2}$)	η (mV) at 10 $mA\ cm^{-2}$	Ref
Amorphous NiWS (Glassy Carbon)	56	17.4	210	this work
Amorphous NiWS (FTO)	55	3.5	265	
Amorphous CoWS (Glassy Carbon)	74	13.4	236	
Amorphous CoWS (FTO)	74	3.2	330	
MoS_2 nanoparticles on Au(111)	55	0.31	–	S12
Double-gyroid MoS_2 network	50	0.67	~284*	S13
MoS_2/graphene hybrid	41	~2.4*	~154*	S14
1T-MoS_2 nanosheets	43	~0.51*	195	S15
Amorphous MoS_3 film	40	0.13	~211*	S16
WS_2 particles	135	~3.2*	–	S17
WS_2 nanosheets	72	2.5	~151*	S18
WS_2 nanoribbons	68	12.5	225	S19
WS_2 nanoflakes exfoliated from WS_2 nanotubes	~200	–	~351*	S20
WS_2 nanoparticles on carbon cloth	68	5.8	~215*	S21
Ultrathin WS_2 nanoflakes mixed with carbon black	48	~6.5*	~154*	S22
WS_2/graphene hybrid by hydrothermal reaction	58	~0.69*	~265*	S23
WS_2/graphene hybrid by electrodeposition	67	~0.66*	306	S24
WS_2/Au hybrid	57	–	~367*	S25
1T-WS_2 nanosheets by lithium intercalation	55	~10*	~233*	S26
1T-WS_2 nanosheets by microwave-assisted intercalation	70	~74*	151	S27

(*) Calculated or read based on their data.

References

[S1] R. I. Walton, S. J. Hibble, *J. Mater. Chem.* **1999**, *9*, 1347.

[S2] J. Espino, L. Alvarez, C. Ornelas, J. L. Rico, S. Fuentes, G. Berhault, G. Alonso, *Catal. Lett.* **2003**, *90*, 71.

[S3] W. Eltzner, M. Breysse, M. Lacroix, M. Vrinat, *Polyhedron* **1986**, *5*, 203.

[S4] A. Müller, E. Diemann, R. Jostes, H. Bögge, *Angew. Chem. Int. Ed.* **1981**, *20*, 934.

[S5] P. D. Tran, S. Y. Chiam, P. P. Boix, Y. Ren, S. S. Pramana, J. Fize, V. Artero, J. Barber, *Energy Environ. Sci.* **2013**, *6*, 2452.

[S6] C. G. Morales-Guio, X. L. Hu, *Acc. Chem. Res.* **2014**, *47*, 2671.

[S7] T. W. Lin, C. J. Liu, J. Y. Lin, *Appl. Catal., B* **2013**, *134*, 75.

[S8] A. B. Laursen, S. Kegnæs, S. Dahl, I. Chorkendorff, *Energy Environ. Sci.* **2012**, *5*, 5577.

[S9] E. J. Popczun, J. R. McKone, C. G. Read, A. J. Biacchi, A. M. Wiltrout, N. S. Lewis, R. E. Schaak, *J. Am. Chem. Soc.* **2013**, *135*, 9267.

[S10] J. D. Benck, Z. B. Chen, L. Y. Kuritzky, A. J. Forman, T. F. Jaramillo, *ACS Catal.* **2012**, *2*, 1916.

[S11] P. Johari, V. B. Shenoy, *ACS Nano* **2011**, *5*, 59038.

[S12] T. F. Jaramillo, K. P. Jørgensen, J. Bonde, J. H. Nielsen, S. Horch, I. Chorkendorff, *Science* **2007**, *317*, 100.

[S13] J. Kibsgaard, Z. Chen, B. N. Reinecke, T. F. Jaramillo, *Nat. Mater.* **2012**, *11*, 963.

[S14] Y. G. Li, H. L. Wang, L. M. Xie, Y. Y. Liang, G. S. Hong, H. J. Dai, *J. Am. Chem. Soc.* **2011**, *133*, 7296.

[S15] M. A. Lukowski, A. S. Daniel, F. Meng, A. Forticaux, L. S. Li, S. Jin, *J. Am. Chem. Soc.* **2013**, *135*, 10274.

[S16] D. Merki, S. Fierro, H. Vrubel, X. L. Hu, *Chem. Sci.* **2011**, *2*, 1262.

[S17] J. Bonde, P. G. Moses, T. F. Jaramillo, J. K. Nørskov, I. Chorkendorff, *Faraday Discuss.* **2008**, *140*, 219.

[S18] Z. Z. Wu, B. Z. Fang, A. Bonakdarpour, A. K. Sun, D. P. Wilkinson, D. Z. Wang, *Appl. Catal., B* **2012**, *125*, 59.

[S19] J. Lin, Z. W.Peng, G. Wang, D. Zakhidov, E. Larios, M. J. Yacaman, J. M. Tour, *Adv. Energy Mater.* **2014**, 4, 1301875.

[S20] C. L. Choi, J. Feng, Y. G. Li, J. Wu, A. Zak, R. Tenne, H. J. Dai, *Nano Res.* **2013**, *6*, 921.

[S21] T. Y. Chen, Y. H. Chang, C. L. Hsu, K. H. Wei, C. Y. Chiang, L. J. Li, *Int. J. Hydrogen Energy* **2013**, *38*, 12302.

[S22] L. Cheng, W. J. Huang, Q. F. Gong, C. H. Liu, Z. Liu, Y. G. Li, *Angew. Chem. Int. Ed.* **2014**, *53*, 7860.

[S23] J. Yang, D. Voiry, S. J.Ahn, D. Kang, A. Y. Kim, M. Chhowalla, H. S. Shin, *Angew. Chem. Int. Ed.* **2013**, *52*, 13751.

[S24] Z. H. Pu, Q. Liu, A. M. Asiri, A. Y. Obaid, X. P. Sun, *Electrochim. Acta* **2014**, *134*, 8.

[S25] J. Kim, S. Byun, A. J. Smith, J. Yu, J. X. Huang, *J. Phys. Chem. Lett.* **2013**, *4*, 1227.

[S26] D. Voiry, H. Yamaguchi, J. W. Li, R. Silva, D. C. B. Alves, T. Fujita, M. W. Chen, T. Asefa, V. B. Shenoy, G. Eda, M. Chhowalla, *Nat. Mater.* **2013**, *12*, 850.

[S27] M. A. Lukowski, A. S. Daniel, C. R. English, F. Meng, A. Forticaux, R. J. Hamers, S. Jin, *Energy Environ. Sci.* **2014**, *7*, 2608.